Hypothalamic neuroglial plasticity is regulated by anti-Müllerian hormone and disrupted in polycystic ovary syndrome

Anne-Laure Barbotin,[a,b] Nour El Houda Mimouni,[a] Grégory Kuchcinski,[a,c] Renaud Lopes,[c] Romain Viard,[d] Sowmyalakshmi Rasika,[a] Daniele Mazur,[a] Mauro S. B. Silva,[a] Virginie Simon,[a] Angèle Boursier,[a,b] Jean-Pierre Pruvo,[c] Qiang Yu,[e] Michael Candlish,[e] Ulrich Boehm,[e] Federica Dal Bello,[f] Claudio Medana,[f] Pascal Pigny,[g] Didier Dewailly,[a] Vincent Prevot,[a] Sophie Catteau-Jonard,[a,h] and Paolo Giacobini[a,*]

[a]Univ. Lille, Inserm, CHU Lille, U1172 - LilNCog - Lille Neuroscience & Cognition, Lille F-59000, France
[b]CHU Lille, Institut de Biologie de la Reproduction-Spermiologie-CECOS, Lille F-59000, France
[c]CHU Lille, Department of Neuroradiology, Lille F-59000, France
[d]Univ. Lille, CNRS, Inserm, CHU Lille, Institut Pasteur de Lille, US 41 - UAR 2014 - PLBS, Lille F-59000, France
[e]Experimental Pharmacology, Center for Molecular Signalling (PZMS), Saarland University School of Medicine, Homburg 66123, Germany
[f]Department of Molecular Biotechnology and Health Science, University of Turin, Turin 10125, Italy
[g]CHU Lille, Service de Biochimie et Hormonologie, Centre de Biologie Pathologie, Lille F-59000, France
[h]CHU Lille, Service de Gynécologie Médicale, Hôpital Jeanne de Flandre, Lille F-59000, France

eBioMedicine
2023;90: 104535
Published Online xxx
https://doi.org/10.1016/j.ebiom.2023.104535

Summary

Background Polycystic ovary syndrome (PCOS) is the most common reproductive-endocrine disorder affecting between 5 and 18% of women worldwide. An elevated frequency of pulsatile luteinizing hormone (LH) secretion and higher serum levels of anti-Müllerian hormone (AMH) are frequently observed in women with PCOS. The origin of these abnormalities is, however, not well understood.

Methods We studied brain structure and function in women with and without PCOS using proton magnetic resonance spectroscopy (MRS) and diffusion tensor imaging combined with fiber tractography. Then, using a mouse model of PCOS, we investigated by electron microscopy whether AMH played a role on the regulation of hypothalamic structural plasticity.

Findings Increased AMH serum levels are associated with increased hypothalamic activity/axonal-glial signalling in PCOS patients. Furthermore, we demonstrate that AMH promotes profound micro-structural changes in the murine hypothalamic median eminence (ME), creating a permissive environment for GnRH secretion. These include the retraction of the processes of specialized AMH-sensitive ependymo-glial cells called tanycytes, allowing more GnRH neuron terminals to approach ME blood capillaries both during the run-up to ovulation and in a mouse model of PCOS.

Interpretation We uncovered a central function for AMH in the regulation of fertility by remodeling GnRH terminals and their tanycytic sheaths, and provided insights into the pivotal role of the brain in the establishment and maintenance of neuroendocrine dysfunction in PCOS.

Funding INSERM (U1172), European Research Council (ERC) under the European Union's Horizon 2020 research and innovation program (grant agreement n° 725149), CHU de Lille, France (Bonus H).

Keywords: PCOS; AMH; GnRH; Tanycytes; MR spectroscopy; Hypothalamus

Introduction

Reproduction in vertebrates depends on the function of hypothalamic neurons that secrete gonadotropin-releasing hormone (GnRH). These neurons send projections to the median eminence (ME), where GnRH is released into the pituitary portal blood vessels for delivery to the anterior pituitary to elicit the secretion of luteinizing hormone (LH) and follicle stimulating

Abbreviations: PCOS, Polycystic Ovary Syndrome; AMH, Anti-Müllerian Hormone; GnRH, Gonadotropin Releasing Hormone; MR, Magnetic Resonance

*Corresponding author.
E-mail address: paolo.giacobini@inserm.fr (P. Giacobini).

Research in context

Evidence before this study

Evidence to date suggests that enhanced GnRH/LH pulsatile release and circulating AMH levels are associated with the neuroendocrine and reproductive impairments of PCOS. The pattern of GnRH secretion, which is exactly mirrored by LH secretion, is episodically pulsatile in mammals, a characteristic essential to properly coordinate gonadal function. Under conditions requiring low gonadotropin output, such as the diestrous phase of the rodent estrous cycle, GnRH-secreting nerve terminals become completely ensheathed by the endfeet of tanycytes, preventing their access to pituitary portal vessels and creating a diffusion barrier for GnRH. Most women with PCOS exhibit accelerated LH pulsatility, which exacerbates androgen production by ovarian theca cells. However, the origin of these abnormalities is not well understood and studies in human patients focusing on possible hypothalamic morphological changes and/or activity in women with PCOS are lacking.

Added value of this study

We investigated brain structure and function in PCOS patients using proton magnetic resonance spectroscopy and diffusion tensor imaging combined with fiber tractography to explore whether hypothalamic dysfunctions could lie at the root of PCOS. Moreover, we took advantage of animal models to mechanistically dissect the central role of AMH. Our findings demonstrate that hypothalamic activity and/or axonal-glial signalling in women with PCOS is increased as compared to control women. In preclinical investigations, using *in vitro* and *ex-vivo* approaches, we have uncovered a central role for AMH in the regulation of GnRH secretion by the control of cytoskeletal plasticity in tanycytes, by inducing the rapid retraction of AMHR2-expressing tanycytic endfeet, thus allowing GnRH neuron terminals to contact the pericapillary space and release the hormone at the level of the pituitary portal vessels.

Implications of all the available evidence

We provide insights into the pathophysiology of PCOS and identify molecular pathways that could become future therapeutic targets for the treatment of this syndrome. Finally, we also uncover the potential for structural and metabolic MRI in the hypothalamus as important tools for better understanding the pathophysiology of PCOS.

hormone (FSH).[1] The pattern of GnRH secretion, which is exactly mirrored by LH secretion, is episodically pulsatile, a characteristic essential to properly coordinate gonadal function.[2] The episodic nature of GnRH release is controlled in part by the structural plasticity of a population of glial cells in the ME, named tanycytes.[3–5] Under conditions requiring low gonadotropin output, such as the diestrous phase of the rodent estrous cycle, GnRH-secreting nerve terminals become completely ensheathed by the endfeet of tanycytes, preventing their access to pituitary portal vessels and creating a diffusion barrier for GnRH.[4,6,7] During the preovulatory GnRH/LH surge on the day of proestrus, tanycytes retract their endfeet, resulting in the release of the ensheathed neuronal terminals and the reestablishment of neurohemal contact, allowing GnRH to enter the pituitary portal blood.[3,5,6] Alterations in the GnRH neural network are associated with a number of reproductive disorders.[8,9] Among these, polycystic ovary syndrome (PCOS) is the most common female reproductive and endocrine syndrome, affecting 10–18% of women of reproductive age worldwide.[10–13] Women with PCOS are characterized by excessive ovarian and/or adrenal androgen secretion, oligo-anovulation, impaired fertility and, in many cases, insulin resistance and associated metabolic perturbations.[11,14,15] Most women who are diagnosed with PCOS also exhibit accelerated LH pulsatility,[16–18] which exacerbates androgen production by ovarian theca cells.[19] This modified LH pulsatility suggests that the frequency of GnRH pulses is elevated as well, and preclinical studies point to central alterations in the hypothalamic network regulating GnRH production and neuronal activity as the culprits behind the neuroendocrine pathophysiology of PCOS.[20–23] However, studies in human patients focusing on possible hypothalamic morphological changes and/or activity in women with PCOS are lacking.

A more recent discovery in the search for the etiology of PCOS is the involvement of anti-Müllerian hormone (AMH).[20,24] AMH is a member of the TGF-beta family,[25] synthesized and produced by the granulosa cells of small antral and preantral follicles[26] and released into the general circulation, suggesting that it might have a hormonal function in a variety of tissues and organs expressing the exclusive binding-receptor AMHR2.[27]

Plasma AMH levels are 2- to 3-fold higher in PCOS patients than in women with normal ovaries,[28,29] and increased AMH levels have been documented during pregnancy in women with PCOS compared with weight-matched non-PCOS controls.[20,30] Recent evidence has also shown that GnRH neurons express AMHR2, both in mice and humans, and preclinical data showed that exogenous AMH potently increases GnRH neuron electrical activity and GnRH release.[24]

In this study, we first studied brain structure and function in PCOS patients using proton magnetic resonance spectroscopy (MRS)[31] and diffusion tensor imaging combined with fiber tractography to explore whether hypothalamic dysfunctions could lie at the root of PCOS. Then, using a mouse model of PCOS, we further investigated whether AMH played a role on the tanycytic structural plasticity, and whether these actions are implicated in the pathophysiology of the condition.

Methods

Human subjects

The MRI study included 17 healthy volunteers and 23 women with PCOS. Patients were included in the PCOS group according to the modified Rotterdam criteria[32,33] by at least 2 of the following 3 criteria: (i) menstrual cycles irregularities, defined by oligo-spaniomenorrhea or amenorrhea, (ii) clinical or biological hyperandrogenism (HA) (total testosterone ≥0.39 ng/ml and/or androstenedione assay ≥1.75 ng/ml and/or Ferriman and Gallwey score ≥6 or severe acne in at least two areas of the body), (iii) morphological appearance of polycystic ovarian morphology on ultrasound (PCOM): ovarian volume >10 cm^3, or ovarian surface area >5.5 cm^2 or at least 20 follicles of 2–9 mm per ovary,[33] and this after excluding all other causes of cycle disorder or hyperandrogenism.

All PCOS women included in this study were women who referred to the gynecology unit for initiation of contraceptive pill, change in contraceptive pill or exhibited hyperandrogenism needing antiandrogen treatment (cyproterone acetate and estradiol). All women had no contraindication of oral contraceptive and were already taking a contraceptive pill or wished to take estroprogestative contraception.

Among the 23 women with PCOS included into the Magnetic Resonance Imaging (MRI) protocol, 11 were under contraceptive treatment. Among the 17 healthy volunteers, 10 were under contraceptive treatment.

Among the 23 women with PCOS included into the MRI protocol, ten women exhibited the full-blown phenotype (also named phenotype A which combine clinical or biochemical HA, oligo-anovulation and PCOM), one woman exhibited phenotype B (HA+oligo-ovulation), two women exhibited phenotype C (ovulatory phenotype combining HA+PCOM) and ten women with phenotype D (non-hyperandrogenic phenotype combining oligo-anovulation with PCOM). All controls women had a history of regular menses (25–35 days) and exhibited no sign of hyperandrogenism. All women (PCOS and controls) included in this study were aged from 18 to 30, and had a body mass index (BMI) comprised between 19 and 30 kg/m^2.

For sample size determination, we used https://clincalc.com/stats/samplesize.aspx software. In our previous work[31] we found a significant difference ($P = 0.015$) between the apparent diffusion coefficients of the mediobasal hypothalamus measured at two times of the menstrual cycle (at D13 or D14 of an artificial cycle under the contraceptive pill, and at the 5th day of the stop period) in 10 healthy female volunteers (observed difference of $85.10^{-5}.mm^2s^{-1}$ with a standard deviation of $99.10^{-5}.mm^2s^{-1}$). Based on these results, to show a difference of at least $85.10^{-5}.mm^2s^{-1}$ between patients and controls, with a standard deviation of $100.10^{-5}.mm^2s^{-1}$, a power of 80% and a first-species risk of 5%, the sample size for each group was set at or above 16 women/group. In order to compensate for possible problems (trial dropout, missing data...), we have recruited 26 subjects per group but several women were removed from the study for various reasons (i.e., patients taking continuous contraception, fortuitous discovery of a drop in ovarian reserve, or dropout from the clinical investigation). At the end of the study, we could analyse the data from 17 healthy volunteers and 23 women with PCOS. Taking into account the stringent screening of the population of subjects to restrict as much as possible inter-individual variability, the final sample size of the two groups ensured adequate power to detect significant differences while also allowing for natural variation in responses. All women included were non-smokers, were tested for illicit drug use the day of the MRI to avoid any cofounding effects on the hypothalamus, and were tested for eventual pregnancy (human chorionic gonadotropin, hCG, measurement). All women included exhibited normal thyroid function and were not diabetic (confirmed by assessment of thyroid stimulating hormone, TSH, and hemoglobin A1C, HbA1C, the day of the 1st MRI). They were asked not to run >10 kms the day before and the day of MRI.

Investigative protocol

The participants had the MRI between the 2nd and the 5th day of their natural menstrual cycle or, in cases of daily estroprogestative contraception treatment, during the last day of their pill-free period. Blood sampling was performed in the early follicular phase (i.e., between cycle days 2 and 5; either spontaneous or induced by dydrogesterone) or during the last day of their pill-free period. Follicle stimulating hormone (FSH), estradiol (E2) and luteinizing hormone (LH) concentrations were measured by immunoassay using an automatic analyzer (Architect, Abbott Laboratories, USA).

The limit of quantification of each assay was as follows: FSH: 0.2 UI/L; LH 0.5 UI/L and E2: 14 pg/ml. Intra- and inter-assay coefficients of variation were 3.1–5.6% for FSH, 4.3–6.4% for LH, and 12–20% for E2.[34]

Fully automated Access Dxi sandwich chemoluminescent immunoassay (Beckman Coulter) was used to measure serum AMH levels. Its limit of quantification is 0.47 pmol/L. Intra- and inter-coefficients of variation are <2 and <3%, respectively.

For PCOS women with amenorrhea, progesterone was also measured the same day before the MRI in order to confirm the early follicular phase. Magnetic resonance spectroscopy (MRS) scans started at 17:00 pm and lasted 45 min and comprised 1 morphological sequence and 3 functional sequences.

Image acquisition

MRI scans were performed at the University Hospital of Lille on a Philips Achieva 3T scanner (Philips Healthcare, Best, the Netherlands) using a 32-channel phased-

array head coil and a whole-body coil transmission as previously described.[31,35] First, high-resolution three-dimensional T1-weighted images were acquired as a series of 160 sagittal slices, using a Turbo Field Echo sequence (TR = 9.9 ms; TE = 4.6 ms; flip-angle = 8°; voxel size = 1 × 1 × 1 mm^3, FOV = 256 × 256 × 160 mm^3). Then, two diffusion-weighted imaging (DWI) acquisitions were performed using a single-shot Echo-Planar Imaging sequence in normal and reversed phase-encoding polarity, for further distortion correction (TR = 13,000 ms, TE = 60 ms, flip angle = 90°; voxel size = 2 × 2 × 2 mm^3, FOV = 256 × 256 mm^2, 132 slices, acceleration factor of 2, 64 gradient-encoded directions with a b-value of 1000 s/mm^2, one b = 0 s/mm^2 image). Finally, for MRS, two PRESS localized spectra were acquired over hypothalamus and thalamus volumes (TR = 2000 ms, TE = 37 ms, FOV = 10 × 10 × 10 mm^3 and a spectral resolution of 1.95 Hz/point).

MRS spectral analysis

The absolute metabolite concentrations were obtained using the LCmodel[36] quantification algorithm. Within LCmodel, concentrations of metabolites are determined using a linear combination fit of the individual *in vitro* metabolite spectra that comprise the "basis set" to the *in vivo* data, as described in a recent investigation in which we have analysed the hypothalamic structural and functional imbalances in women affected by anorexia nervosa as compared to healthy subjects.[35] The basis set was acquired with long TR and short TE to minimize relaxation effects. Only voxels within the excitation region were presented for LCmodel analysis without any other preprocessing such as zero filling or apodization. Peak registration in LCmodel was performed using the prominent peaks of glutamine, glutamate and creatine observed inside hypothalamus volume of interest (VOI), while using thalamus as control VOI. As performed previously,[35] the spectral analysis window, 3.85 ppm–1.0 ppm was used for 3T data to prevent variability in the results from lipid artifacts that are more prominent at 3T. Spectra were included in the final analysis based on quality criteria defined by objective output parameters from the LCmodel analysis: sufficient spectral resolution (full width at half minimum 0.07 ppm), sufficient information (Signal-to-Noise Ratio, SNR = 4) and residuals that were randomly scattered about zero to indicate a reasonable fit to data. By using the analysis window of 3.85 ppm, deviations in the fit due to baseline distortion from improper water suppression were avoided. All spectra included in the results had smooth and reasonably flat baseline estimates. We employed a double-blind, condition-control, for the analysis. The procedure for quantifying metabolite concentrations consists in fitting the experimental data to a parametric model describing the resonances of each metabolite. Relative Cramér-Rao lower bound (rCRB) is used as a benchmark of precision for the concentration measurements. We set a rejection threshold for CRB at 30%, above which the noise-to-background signal is too high to allow precise measurements of metabolites.

Automatic segmentation and fiber tractography

Segmentation of regions of interest (ROI)

Hypothalamic segmentations were obtained using a convolutional neural network (CNN) to form five subunits comprised of multiple hypothalamic nuclei trained on manually parcellated T1-weigthed images and which are defined as follows: Anterior-inferior (suprachiasmatic nucleus; supraoptic nucleus); Anterior-superior (preoptic area; paraventricular nucleus); Posterior (mamillary body, lateral hypothalamus; tuberomamillary nucleus, TMN); Inferior tuberal (infundibular or arcuate nucleus, ARC; ventromedial nucleus; supraoptic nucleus, SON; lateral tubular nucleus); Superior tuberal (dorsomedial nucleus; paraventricular nucleus, PVN; lateral hypothalamus). The method was previously described[37] and now available in Freesurfer 7.2. Data augmentation was used to limit variability in acquisition parameters and in anatomy. Such approaches enable fast segmentation of large data sets with high accuracy and applicability.

Fiber tractography

Diffusion-weighted imaging, DWI, were corrected for Eddy currents, geometrical and signal distortions and rigidly co-registered with T1 images using HCP toolbox as described in Ref. 38. The obtained transformation matrix was then applied to seeds defined in native T1 space.

DWI data were processed using the MRtrix software (v3.0.1). For each subject, an FA map was calculated and threshold (FA > 0.7) to determine the response function of highly anisotropic voxels, further used for constrained spherical deconvolution to provide sharp fiber orientation distribution (FOD) estimates. Fiber tracts were generated using a probabilistic tracking algorithm. Tracking parameters were left to defaults (step size = 0.1 mm, minimum radius curvature = 1 mm, FOD cutoff = 0.2, minimum length = 10 mm), the maximum harmonic order set to 10 and the number of generated tracts set to 2,000,000. Hypothalamus mask, resampled to the DWI space, was used as seeding mask, while the tracking mask was defined by the 1-mm dilated white matter mask. Finally, fibres going through each hypothalamus subunit were selected to compute fiber density.

Animals

C57BL/6J mice (Charles River, USA) were housed at 21–22 °C with a 12 h light/dark cycle. Standard diet (9.5-mm pelleted RM3, Special Diets Services, France) was given to all mice during breeding, lactation, and growth of young stock. Mice were randomly assigned to groups of five animals per cage at the time of purchase or

weaning with litters within the same treatment allocation group mixed together (pseudo-random mixing based on weight) to minimize any potential bias. No data were excluded from analyses.

tdTomato$^{lox P/+}$ mice (breeding pairs 3–6 months old) were purchased from the Jackson Laboratories (Bar Harbor, ME). *AMHR2-Cre*;*Z/E*$^{lox P/-,\beta geo/+}$ (LacZ/EGFP) knock-in mice mouse strains have been previously described and validated.[39,40]

Prenatal anti-Müllerian Hormone (PAMH) treatment was performed as previously described.[20] Timed-pregnant adult (3–4 months) C57BL6/J (B6) dams were injected daily intraperitoneally (i.p.) from embryonic day (E) 16.5–18.5 with 200 µl of a solution containing respectively: 1) 0.01 M phosphate buffered saline (PBS, pH 7.4, prenatal control-treated), 2) PBS with 0.12 mg Kg^{-1}/d human anti-Müllerian hormone (AMH)-C-terminal protein (AMH_C, R&D Systems, USA; rhMIS 1737-MS-10, prenatal AMH (PAMH-treated).

Rats: Female Sprague Dawley rats (Janvier, Saint-Berthevin, France; 3–4 months old; 250–300 g) were provided ad libitum access to water and standard laboratory chow (Special Diet Services, RM3, France, for mice; Purina lab chow, 5001, USA, for rats). Vaginal smears were examined daily, and only rats that exhibited at least two consecutive 4-d estrous cycles were used for experiments. Diestrus 1 and 2 were defined by the predominance of leukocytes in the vaginal lavage, the day of proestrus was characterized by the predominance of round nucleated epithelial cells, and estrus was distinguished by a large number of clustered cornified squamous epithelial cells.

Murine AMH ELISA

Quantification of AMH in the serum of diestrous female mice was performed using the commercial rat and mouse AMH ELISA kit (Ansh Labs LLC, TX, USA; AL-113) following manufacturer's protocol. Briefly, diluted serum (1/10 for adults) and standards were added to AMH antibody-coated wells and incubated for 2 h at room temperature. After washing, wells were incubated with biotinylated AMH antibody for 1 h, followed by incubation with streptavidin horseradish peroxidase conjugate for 30 min. Then, the plate was developed using tetramethylbenzidine (TMB) and the light absorbance was read at 450 nm using a microplate reader (SpectraMax i3, molecular devices, San José, CA, USA). Limit of ELISA sensitivity was 0.34 ng/ml. The calculated intra-assay coefficient of variation of the assay was 10.43%.

Semi-quantification of GnRH in the ME

To determine whether AMH promotes GnRH nerve terminal plasticity, *ex vivo* experiments were carried out according to previously described protocols.[4–6] Female PAMH mice (P90) and PBS controls mice were killed on diestrus by decapitation. After rapid removal of the brain, hypothalamic explants were microdissected without damaging the MEs. Explants were then processed for electron microscopy as described previously[4–6] and immunostained for GnRH as detailed below. Tissues were fixed by immersion in a solution of 2% paraformaldehyde, 0.2% picric acid, and 0.1% glutaraldehyde in 0.1 M phosphate buffer, pH 7.4, for 2 h at 4 °C. Tissues were post fixed with 1% OsO4 in phosphate buffer for 1 h at room temperature. After dehydration, tissues were embedded in Araldite. Semithin sections (1–2 µm thick) were used to progressively approach and identify the portion of the ME targeted for ultrastructural studies—that is, the area where the pituitary stalk becomes distinct from the base of the hypothalamus but still remains attached to it by the hypophyseal portal vasculature.[6] This area, which does not extend beyond 20 µm, contains high numbers of GnRH fibers. To detect GnRH immunoreactivity, ultrathin sections (80–90 nm thick) collected on Parlodion 0.8%/isoamyl acetate-coated 100 mesh grids (EMS, Fort Washington, PA, USA) were treated using an immunogold procedure described previously.[6] After a preliminary treatment with H_2O_2 (10%; 8 min) and a blocking step in TBS (0.1 M Tris, pH 7.4, 0.15 M NaCl) containing 1% normal goat serum and 1% bovine albumin serum (TBSB) (10 min at room temperature), the grids were floated on a drop of the following reagents and washing solutions: (1) rabbit anti-GnRH (1:5000) in TBSB for 60 h at 4 °C, (2) TBS to remove excess antibodies (three times for 10 min), (3) colloidal gold (18 nm)-labeled goat anti-rabbit immunoglobulins (Jackson ImmunoResearch Laboratories, Inc.) 1:20 in TBS for 90 min at room temperature, (4) TBS (three times for 10 min), and (5) distilled water (three times for 10 min). The sections were then counterstained with uranyl acetate and lead citrate before observation. The specificity of the GnRH antiserum used has been previously validated.[41] Moreover, specificity of the immunostaining was verified by omission of the primary antibody. Images were acquired using a Gatan Orius SC1000 CCD camera (Gatan France, Grandchamp, France). Morphometric analysis was performed by an investigator blind to hypothalamic explant treatment on digitalized images taken at an original magnification of 12,000× from 10 to 15 ultrathin sections per animal, with a space of 25 sections between them, to avoid taking the same GnRH nerve terminal into consideration twice (the diameter of a GnRH nerve terminal rarely exceeds 2 µm). All GnRH-immunoreactive nerve terminals located at less than 10 µm from the parenchymatous basal lamina (i.e., the pial surface of the brain) were taken into consideration—that is, more than 100 distinct axon terminals per animals (i.e., almost all GnRH nerve terminals abutting onto the pituitary portal blood vessels in the aforementioned 20-µm-thick region of the ME). The number of immunogold particles per μm^2 was calculated and was considered to be proportional to the GnRH content.

Assessment of ultrastructural changes in the ME of rats

To determine whether AMH promotes GnRH nerve terminal plasticity, *ex vivo* experiments were carried out according to previously described protocols.[42] Female rats (3 months old, 250–300 g) were killed on diestrus 2 by decapitation. After rapid removal of the brain, hypothalamic explants were microdissected without damaging the MEs. Explants were placed in 12-well plates and preincubated for 30 min at 37 °C in 1 ml of Krebs–Ringer bicarbonate buffer, pH 7.4, containing 4.5 mg/ml D-dextrose and 5 μM tetrodotoxin, under an atmosphere of air containing 5% CO^2. After this preincubation, tissues were placed in fresh medium with or without AMH_C (1 μg/ml; rhMIS 1737-MS-10, R&D Systems, MN, USA) for an additional 30 min incubation period. Explants were then processed for electron microscopy as described previously[6] and detailed above in the "semi-quantification of GnRH in the ME" chapter. The sections were then counterstained with uranyl acetate and lead citrate before observation. The specificity of the GnRH antisera used has been discussed previously.[6] Ultrathin immunolabeled sections were examined with a Zeiss transmission electron microscope 902 (Leo, Rueil-Malmaison, France), and images were acquired using a Gatan Orius SC1000 CCD camera (Gatan France, Grandchamp, France). Morphometric analysis was performed by an investigator blind to hypothalamic explant treatment on digitalized images taken at an original magnification of 12,000× from 10 to 15 ultrathin sections per animal, with a space of 25 sections between them, to avoid taking the same GnRH nerve terminal into consideration twice (the diameter of a GnRH nerve terminal rarely exceeds 2 μm). All GnRH-immunoreactive nerve terminals located at less than 10 μm from the parenchymatous basal lamina (i.e., the pial surface of the brain) were taken into consideration —that is, more than 100 distinct axon terminals per animals (i.e., almost all GnRH nerve terminals abutting onto the pituitary portal blood vessels in the aforementioned 20-μm-thick region of the ME). Immunolabeled terminals confined to a distance of 10 μm or less from the basal lamina were imaged and the distance from the nerve terminal to the pericapillary space recorded. The number of immunoreactive terminals (GnRH nerve terminals), the area occupied by tanycytes and the number of gold particles per μm^2 of nerve terminals were expressed as mean (±S.E.M.).

We chose to use ME from rats, and not from mice, to assess *ex vivo* the direct effect of AMH on structural plasticity, to be coherent with the *in vitro* functional experiments described in "tanycytic cell culture", which had to be performed in rats for the reasons detailed below.

Tat-cre injection

C57BL/6J mice female mice (3 months old) and *tdTomato*$^{loxP/+}$ female mice (3–6 months old) were placed in a stereotactic frame (Kopf Instruments, CA, USA) under anaesthesia (isoflurane) and a burr hole was drilled 1.7 mm posterior to the Bregma. A 10-ml Hamilton syringe was slowly inserted into the third ventricle (5.6-mm deep relative to the dura) and 1.5 ml of Tat-cre (2.1 mg ml^{-1}) was injected using an infusion pump over 5 min. The Tat-cre fusion protein produced as detailed previously.[43]

Isolation of hypothalamic tanycytes using fluorescence activated cell sorting

Mediobasal hypothalamus (MBH) from Tat-cre-injected *tdTomato*$^{loxP/+}$ female mice (3–6 months old) fed ad libitum were microdissected and enzymatically dissociated using a Papain Dissociation System (Worthington Biochemical Corporation, Lakewood, NJ, USA), to obtain single-cell suspensions as previously described.[4] FACS analysis was performed using an EPICS ALTRA Cell Sorter Cytometer device (Beckman Coulter, Inc., CA, USA). The sorting decision was based on measurements of tdTomato fluorescence (excitation: 488 nm; detection: bandpass 675 ± 20 nm) by comparing cell suspensions from tdTomato-positive and wild-type animals. For each animal, 5000–8000 tdTomato-positive cells were sorted directly into 10 μl extraction buffer: 0.1% Triton X-100 (Sigma–Aldrich, USA) and 0.4 Uμl^{-1} RNase OUT TM (Life Technologies, USA).

Quantitative RT-PCR analyses

For gene expression analyses, mRNAs obtained from FACS-sorted tanycytes were reverse transcribed using SuperScript® IV Reverse Transcriptase (Life Technologies, USA) and a linear preamplification step was performed using the TaqMan PreAmp Master Mix Kit protocol (P/N 4366128, Applied Biosystems, USA) as previously described.[4] Real-time PCR was carried out on an Applied Biosystems 7900HT Fast Real-Time PCR System, using exon-boundary-specific TaqMan Gene Expression Assays (Applied Biosystems, USA) as follows: *Amh* (Amh-Mm00431795_g1), *Amhr2* (Amhr2-Mm00513847_m1). Control housekeeping genes were *r18S* (18S: Hs99999901_s1) and *Actb* (Actb: Mm00607939_s1). Gene expression data were analysed using SDS 2.4.1 and Data Assist 3.0.1 software (Applied Biosystems, USA). Values are expressed relative to control values, as appropriate, set at 1.

Tissue preparation

Adult female mice (P60–P90) were anesthetized with i.p. injections of 100 mg/kg of ketamine-HCl and 10 mg/kg xylazine-HCl and perfused transcardially with 20 ml of saline, followed by 100 ml of 4% PFA in 0.1 M phosphate buffer (PB) (4% PFA/0.1 M PB; pH 7.6). Brains were collected, postfixed in the same fixative for 2 h at 4 °C, cryoprotected overnight in PB/sucrose 30% at 4 °C, embedded in OCT embedding medium (Tissue-

Tek, Sakura Finetek, Japan), and frozen and stored at –80 °C until cryosectioning.

Immunohistochemistry

Tissues were cryosectioned coronally (Leica Biosystems, Germany CM3050S) at 35 µm for free-floating immunohistochemistry (IHC). Sections were blocked in an incubation solution of Tris-buffered saline (TBS 0.05 M, pH 7.6), 0.25% bovine serum albumin (BSA; Sigma–Aldrich, USA; A9418), 0.3% Triton X-100 (TBS-T; Sigma–Aldrich, USA; T8787) with 10% normal donkey serum (NDS; D9663; Sigma–Aldrich, USA) for 2 h at room temperature before incubation with the primary antisera (depending on experiment) for 48 h at 4 °C.[20] After TBS rinses, immunoreactivity was revealed using the corresponding secondary antibodies (Molecular Probes, ThermoFisher Scientific, USA) all 1:400, [Alexa-Fluor 488-conjugated #A21206; Alexa-Fluor 568-conjugated #A10042, #A10037] for 90 min in incubation solution at RT. After TBS washes, sections were incubated with 0.02% Hoechst (H3569; Sigma–Aldrich, USA) in TBS-T for 15-mins at RT and mounted on gelatin-coated slides and coverslipped with mowiol medium (Sigma–Aldrich, USA; #81381). Sections were examined using an Axio Imager, Z1 ApoTome microscope (Carl Zeiss, Germany) equipped with a motorized stage, and an AxioCam MRm camera (Zeiss, Germany). For confocal observation and analyses, an inverted laser-scanning Axio observer microscope (LSM 710, Zeiss, Germany) with an EC Plan NeoFluar 100×/1.4 numerical aperture oil-immersion objective (Zeiss, Germany) was used with an argon laser exciting at 488 nm and helium laser exciting at 543 nm (Imaging Core Facility of IFR114, of the University of Lille 2, France).

Primary antibody list for immunohistochemistry

Rabbit polyclonal anti-AMH C-terminal (Abcam, UK; ab229212; 1:1000); rabbit polyclonal anti-AMHR2 (CASLO, custom made 56G, 1:2000)[24]; rabbit polyclonal anti-GFP (Abcam, UK; ab6556; 1:1000); rabbit polyclonal anti-cFos (Santa Cruz Biotechnology, USA; #sc-52; 1:5000); chicken anti-vimentin, (Millipore, Germany; AB5733, 1:2000); guinea pig anti-GnRH (EH#1018, 1:10,000), a generous gift from Dr. Erik Hrabovszky (Laboratory of Endocrine Neurobiology, Institute of Experimental Medicine of the Hungarian Academy of Sciences, Budapest, Hungary) and previously validated.[44] Phalloidin (1:100) was used to stain actin cytoskeleton of fixed and permeabilized cells (Life Technologies, Molecular Probes, Invitrogen, USA). For immunogold experiments, a rabbit polyclonal anti-GnRH (1:5000), which was previously validated in similar experiments,[4,6] was used. This antibody was a generous gift from Professor G. Tramu (Centre Nationale de la Recherche Scientifique, URA 339, Université de Bordeaux I, Talence, France). Information on the antibodies used is listed in Table S1.

Tanycyte cell culture

Tanycyte cell cultures were performed as previously described.[4,45] Primary cultures of tanycytes were prepared using MEs dissected from 10-day-old rats. Microdissected tissues from a minimum of 10 rat pups were pooled in ice-cold DMEM (Sigma–Aldrich). The tissues were dissociated and the cell suspension was transferred to a 25 cm culture flask (Sigma–Aldrich) with an additional 5 ml of supplemented medium. Rats were used instead of mice to generate primary tanycytic cultures because the bigger size of the ME in P10 rat pups as compared to P10 mouse pups allows a better culture yield.

After a growing period of 8–10 days in 75 cm^2 culture flasks containing DMEM F-12 high-glucose medium supplemented with 10% calf serum and 2 mM L-glutamine, tanycytes were isolated from contaminant cells by overnight shaking at 250 r.p.m. and were plated either in 15 cm^2 dishes (1–1.5 million cells per dish) for immunoblot analysis or on coated coverslips in six-well plates for immunohistochemistry. After reaching 90% confluence, the medium was replaced with a serum-free, tanycyte defined medium consisting of DMEM devoid of phenol red, supplemented with 2 mM L-glutamine, 15 mM HEPES, 5 µg/ml insulin and 100 µM putrescine. The cells were used 48 h later for experiments.

Western blotting

Rat cultured tanycytes were boiled for 5 min after thawing and electrophoresed for 75 min at 150 V for 75 min in precast 3%–8% SDS–polyacrylamide Tris-acetate gels according to the protocol supplied with the NuPAGE system (Invitrogen). After size-fractionation, the proteins were transferred onto Nitrocellulose membranes (0.2 mm pore-size membranes; LC2002; Invitrogen) in the blot module of the NuPAGE system (Invitrogen, USA) for 75 min at RT. Blots were blocked for 1 h in TBS with 0.05% Tween 20 (TBST) and 5% non-fat milk at RT, incubated overnight at 4 °C with their respective primary antibodies and washed four times with TBST before being exposed to horseradish peroxidase-conjugated secondary antibodies diluted in 5% non-fat milk-TBST for 1 h at RT. The immunoreactions were detected with enhanced chemiluminescence (NEL101, PerkinElmer, Boston, MA, USA).

The goat anti-AMH (AF2748; 1:100) and the goat anti-AMHR2 (AF1618; 1:400) antibodies were purchased from R&D Systems, USA. Immunoreactions were detected with horseradish peroxidase-conjugated secondary antibodies (Sigma; USA 1:10,000). Protein

expression was densitometrically analysed using Scion Image software (Scion Corporation, MA, USA).

Wound-healing assay

Primary tanycytes were seeded at a high density (1×10^5 cells/cm^2) into cell culture insert (Ibidi) to generate a wound with a gap of 500 μm. Cells were cultures for 48 h in DMEM F-12 high-glucose medium supplemented with 2% calf serum and 2 mM L-glutamine and treated with PBS (control) or recombinant hAMH (100 ng/ml; rhMIS 1737-MS-10, R&D Systems, USA). Then, the cells were fixed in 4% PFA in 0.1 M phosphate buffer (PB) (4% PFA/0.1 M PB; pH 7.6) and permeabilized with 0.3% Triton X-100 (TBS-T; Sigma–Aldrich, USA, T8787) for 1 h before staining of the actin cytoskeleton using Alexa Fluor 568 Phalloidin (1:100; ThermoFisher Scientific, USA, A12380). The area occupied by tanycytic processes was measured using ImageJ software (Bethesda, USA).

Ethics statement

Human studies

The human study was performed in accordance with the Declaration of Helsinki. All participants gave written informed consent prior to inclusion in the study. The study was carried out with the approval of regional ethics committee (Comité de Protection des Personnes Nord Ouest IV; No: 2016-A01391-50). The clinical protocols have been declared at ClinicalTrials.gov (Identifier: NCT03043924).

Animal studies

8Animal studies were approved by the Institutional Ethics Committees of Care and Use of Experimental Animals of the Universities of Lille 2 (France). All experiments were performed in accordance with the guidelines for animal use specified by the European Union Council Directive of September 22, 2010 (2010/63/EU) and the approved protocol (APAFIS# 29172-2020121811279767 v5) by the Ethical Committee of the French Ministry of Education and Research. Animal studies were conducted in accordance with the ARRIVE (Animal Research: Reporting of *In Vivo* Experiments) guidelines.[46]

All efforts were made to minimize animal suffering and animal care was supervised by veterinarians and animal technicians skilled in rodent healthcare and housing.

Statistics

All statistical analyses were performed, as previously described,[20] using Prism 7 (GraphPad Software) and assessed for normality (Shapiro–Wilk test) and variance when appropriate. Mouse study: no statistical methods were used to pre-determine sample size, or to randomize. However, analyses were performed by two independent investigators in a blinded fashion and animals were randomly assigned to groups at weaning to minimize any potential bias. Animals were housed in same-sex groups of five animals per cage at weaning, with litters within the same treatment group mixed together (pseudo-random mixing based on weight). For each experiment, replicates are described in the figure legends. No samples were excluded from the analyses. The number of the animals used for each experiment, together with the details of the statistical tests used for the analyses, are indicated in the figure legends of the corresponding figures.

Case-control studies: No randomization. The sample size pre-determination has been detailed above in the "Human subjects" section.

For the human study, we did not perform a multivariate analysis to help adjusting for any potential confounders because the inclusion criteria included stringent parameters: age (18–30), BMI comprised between 19 and 30 kg/m^2, absence of tobacco and drug use (verified by a test on the day of the MRI), which are the main confounding factors for such analysis. Moreover, the great majority of our study cohort was lean, with only 2 patients included having a BMI above 25.

For normally distributed samples, data were compared using an unpaired two-tailed Student's t test or one-way ANOVA for multiple comparisons followed by Tukey's multiple comparison post hoc test. For populations that were not normally distributed, data analyses were performed using either a Wilcoxon–Mann–Whitney test (comparison between two experimental groups) or Kruskal–Wallis test (comparison between three or more experimental groups) followed by a Dunn's post hoc analysis. The numbers of biologically independent experiments, sample size, P values, and ages and sexes of the animals are all indicated in the main text or figure legends. The significance level was set at $P < 0.05$. The correlations between the various parameters were expressed as Spearman's correlation coefficient (r). A P value of <0.05 was considered to be significant and a r absolute value ≥0.4 was considered to be strong and clinically relevant.

Role of funders

The funding sources for this project played no role in the study design, data collection, analysis, interpretation, writing, or editing of the manuscript.

Results

Increased hypothalamic activity in women with PCOS

Since most women with PCOS present increased circulating levels of AMH as compared to controls,[28,29] we first investigated whether these alterations are associated with modifications in hypothalamic structure or function in PCOS patients. Consistent with previous studies,[28,29] we found that women with PCOS had higher AMH levels than healthy women (Table 1).

	Control (n = 17)	PCOS (n = 23)	P
Age (years)	26.34 ± 0.60	24.89 ± 0.76	0.18
BMI (kg/m^2)	22.53 ± 0.64	21.98 ± 0.47	0.46
FSH (UI/L)	5.23 ± 0.37	5.31 ± 0.26	0.74
LH (UI/L)	4.12 ± 0.43	6.08 ± 1.00	0.48
FSH/LH	1.45 ± 0.17	1.41 ± 0.21	0.66
Oestradiol (pg/mL)	37.47 ± 5.78	38.04 ± 4.33	0.79
AMH (pmol/L)*	23.12 ± 2.64	66.67 ± 10.52	<0.0001

Data are mean ± s.e.m. Comparisons between groups were made using the Wilcoxon–Mann–Whitney test. Abbreviations: AMH, anti-Müllerian hormone; BMI, Body mass index; FSH, follicle stimulating hormone; LH, luteinizing hormone; PCOS, polycystic ovary syndrome.

Table 1: **Population characteristics of control women and women with PCOS included in the imaging study.**

We used MRS to measure brain metabolites in aged- and BMI-matched healthy and PCOS women. In order to standardize MRI results between the different groups, participants were subjected to an MRI between the 2nd and 5th day of their natural menstrual cycle or, in case of daily oral contraceptive use, on the last day of their pill-free period.[47]

We then performed voxel-based spectroscopic analyses of freely moving molecules[48] both in the hypothalamus (Fig. 1a) and in the thalamus (Fig. 1b), and normalized the data to total creatine (Cr) in a semi-quantitative approach. Since we cannot differentiate creatine from phospho-creatine using 3T MRI, the reference that we used was total creatine (creatine + phospho-creatine).

We measured a range of cerebral metabolites including N-acetyl-aspartate (NAA), a marker of neuronal integrity, activity and axonal-glial signalling,[49,50] and choline (Cho; Fig. 1c), a marker of membrane metabolism, which is present in all neurons but which has been reported to be present at higher concentrations in glia.[51] When comparing NAA/Cr and Cho/Cr concentration ratios, respectively, we found that the former was higher in the hypothalamus of women with PCOS than in controls (Fig. 1d; control women n = 17, PCOS women n = 23; $P = 0.0034$, Wilcoxon–Mann–Whitney test). In contrast, NAA/Cr ratios in the thalamus were not different between healthy and PCOS women (Fig. 1e; control women n = 17, PCOS women n = 23; $P = 0.21$, Wilcoxon–Mann–Whitney test), suggesting that the metabolic changes observed were specific to the hypothalamus. The Cho/Cr ratio, in contrast, was not different between PCOS and control women in either the hypothalamus (Fig. 1f; control women n = 17, PCOS women n = 23; $P = 0.58$, Wilcoxon–Mann–Whitney test) or the thalamus (Fig. 1g; control women n = 17, PCOS women n = 23; $P = 0.30$, Wilcoxon–Mann–Whitney test). Together, our results indicate increased hypothalamic activity and/or axonal-glial signalling in women with PCOS.

To investigate changes in the microstructure of the hypothalamus that could underlie these functional modifications, we next automatically segmented each hypothalamic region using high-resolution anatomical MRI sequences[37] for all 40 participants individually (Fig. 2a). Each of the hypothalamic segments constituted a region of interest (ROI) for fiber tracking after their co-registration to diffusion-weighted imaging (DWI) space. We then used a probabilistic tractography algorithm to determine the number of fibers passing through each distinct ROI in a single subject[52] (Fig. 2b). The average density of fibers in the left, but not the right, inferior tuberal region was significantly higher in patients with PCOS as compared to healthy women (Fig. 2b and c; control women n = 17, PCOS women n = 23; left tuberal inferior $P = 0.036$, right tuberal inferior $P = 0.51$; unpaired two-tailed Student's t test). No such differences between groups were noted in any other hypothalamic ROIs analysed (Fig. 2c; control women n = 17, PCOS women n = 23; left tuberal superior $P = 1$, right tuberal superior $P = 0.93$, left anterior inferior $P = 0.41$, right anterior inferior $P = 0.91$, left anterior superior $P = 0.80$, right anterior superior $P = 0.60$, left posterior $P = 0.21$, right posterior $P = 0.56$; unpaired two-tailed Student's t test). This specific lateralized asymmetry in the inferior tuberal region, which comprises the infundibular region (arcuate nucleus: ARC and median eminence: ME), might therefore represent alterations in the connectivity of the ARC-ME in women with PCOS and contributing to the neuroendocrine alterations typical of the syndrome.

Altered AMH levels and hypothalamic structural plasticity in a preclinical model of PCOS

In light of the altered hypothalamic connectivity observed in women with PCOS, we next assessed whether a PCOS-like mice model that we recently established by prenatal treatment with high AMH[20] (PAMH model) and which recapitulates in adulthood the major cardinal reproductive and metabolic defects of the human syndrome,[20,53,54] could also mimic the elevated circulating AMH levels seen in PCOS patients (Fig. 3a and b; Table 1). We measured AMH using ELISA in female PAMH mice and controls during the juvenile period (P25), before puberty onset, and during adulthood (P60, diestrus). Consistent with the human condition,[28,29] we found that PAMH mice had higher AMH levels than control animals throughout postnatal life (Fig. 3b; P25 CNTR n = 6, PAMH n = 6, $P = 0.045$, paired two-tailed Student's t test; P60 CNTR n = 9, PAMH n = 11, $P = 0.039$, unpaired two-tailed Student's t test).

Next, we investigated the ultrastructural organization of the hypothalamic ME from CNTR or PAMH mice (P90–P120). Electron microscopic analyses of ME explants from control and PAMH mice at diestrus revealed profound structural alterations in the latter (Fig. 3c and d). The area occupied by tanycytic processes

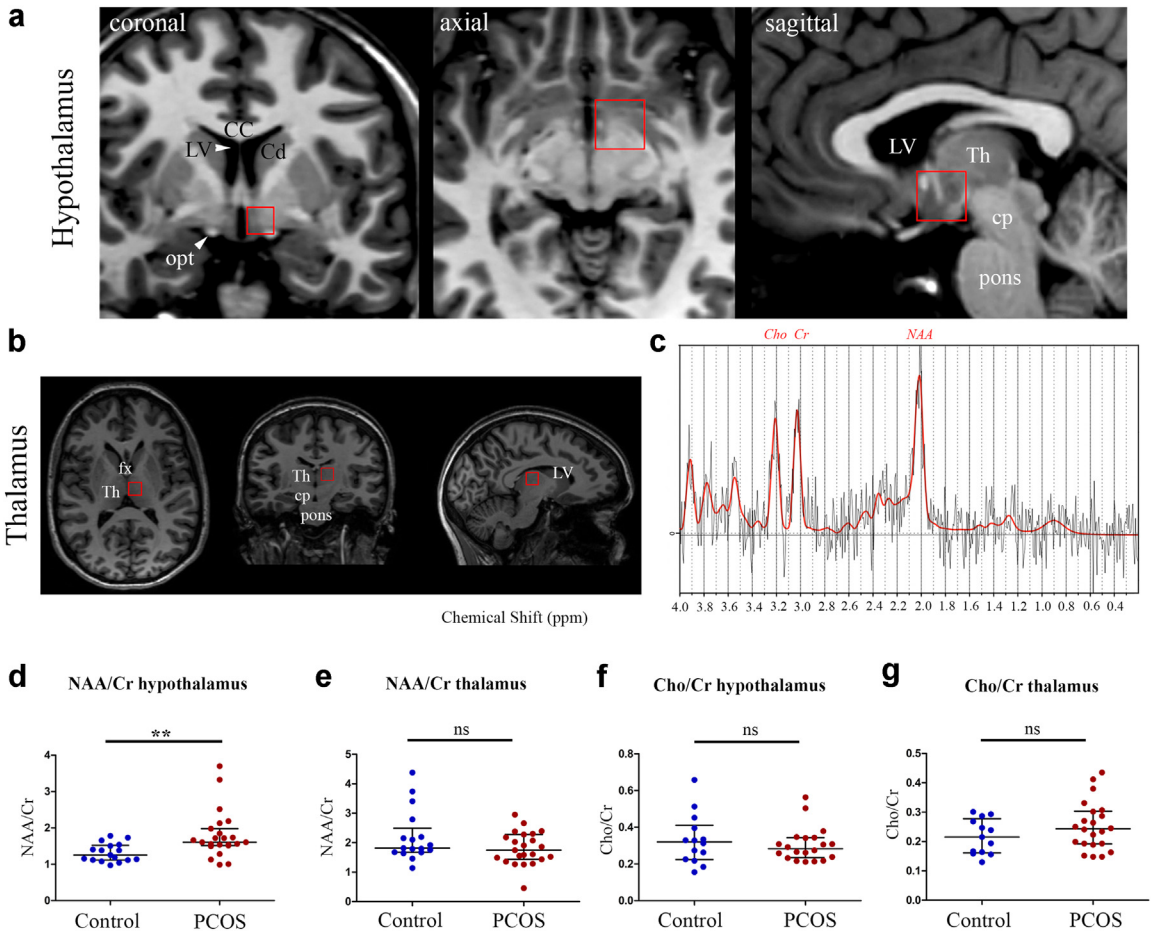

***Fig. 1:* Increased neuronal activity and axon-glial signalling in the hypothalamus of women with PCOS.** Magnetic Resonance Spectroscopy (MRS) analysis of the hypothalamus (**a**) and thalamus (**b**) using the volumes of interest shown in **a** and **b**, respectively. (**c**) Representative typical spectrum of proton MR spectroscopy spectrum of hypothalamus along with molecular assignment of resonances (NAA: N-acetyl-aspartate at 2.02 ppm; Cr: creatine at 3.01 ppm; Cho: choline at 3.22 ppm). (**d** and **e**) Ratio of the concentrations of NAA to total Cr (creatine + phosphocreatine) in the hypothalamus (**d**) and thalamus (**e**) of healthy participants (n = 17) and PCOS volunteers (n = 23). (**f** and **g**) Ratio of the concentrations of Cho to total Cr in the hypothalamus (**f**) and thalamus (**g**) of healthy women (n = 17) and PCOS women (n = 23). $^{**}P < 0.01$, n.s: not significant, Wilcoxon–Mann–Whitney test. The horizontal line in each plot corresponds to the median value. The vertical line represents the 25th–75th percentile range. Abbreviations: CC, corpus callosum; Cd, caudate nucleus; cp, cerebral peduncle; fx, fornix; LV, lateral ventricle; opt, optic tract, Th, thalamus.

(green) at less than 2 µm from the basal lamina was nearly 90% of the total area in control animals but dropped to 67% in PCOS-like animals (Fig. 3e; CNTR n = 5, PAMH n = 3; P = 0.036, Wilcoxon–Mann–Whitney test). This was followed by a significant increase in the percentage of GnRH axonal terminals (blue) located at less than 1 µm from the parenchymatous basal lamina (pink) in the PAMH animals (Fig. 3f; CNTR n = 5, PAMH n = 3; P = 0.036; Wilcoxon–Mann–Whitney test). The choice of this distance for the quantitative morphometric analysis was based on a previous study showing that morphological changes in the ME only occur for the fraction of GnRH terminals present at <1 µm from the basal lamina.[55] As expected, the percentage of GnRH neurons in close proximity to the basal lamina was inversely correlated to the area covered by tanycytic processes at 2 µm or less from the basal lamina (Fig. 3g; r = –0.8, P = 0.015, Spearman's correlation).

We next aimed to determine whether this alteration of hypothalamic neuroglial plasticity was also accompanied by an increase in GnRH content at the level of the axon terminals by immunogold labeling for GnRH (Fig. 3h–l). Analyzing 877 GnRH-immunoreactive axon terminals in controls (n = 5) and 682 GnRH-immunoreactive axon terminals in PAMH mice (n = 3), we found a significantly higher number of 18 nm-gold particles per µm^2 in the GnRH terminals of

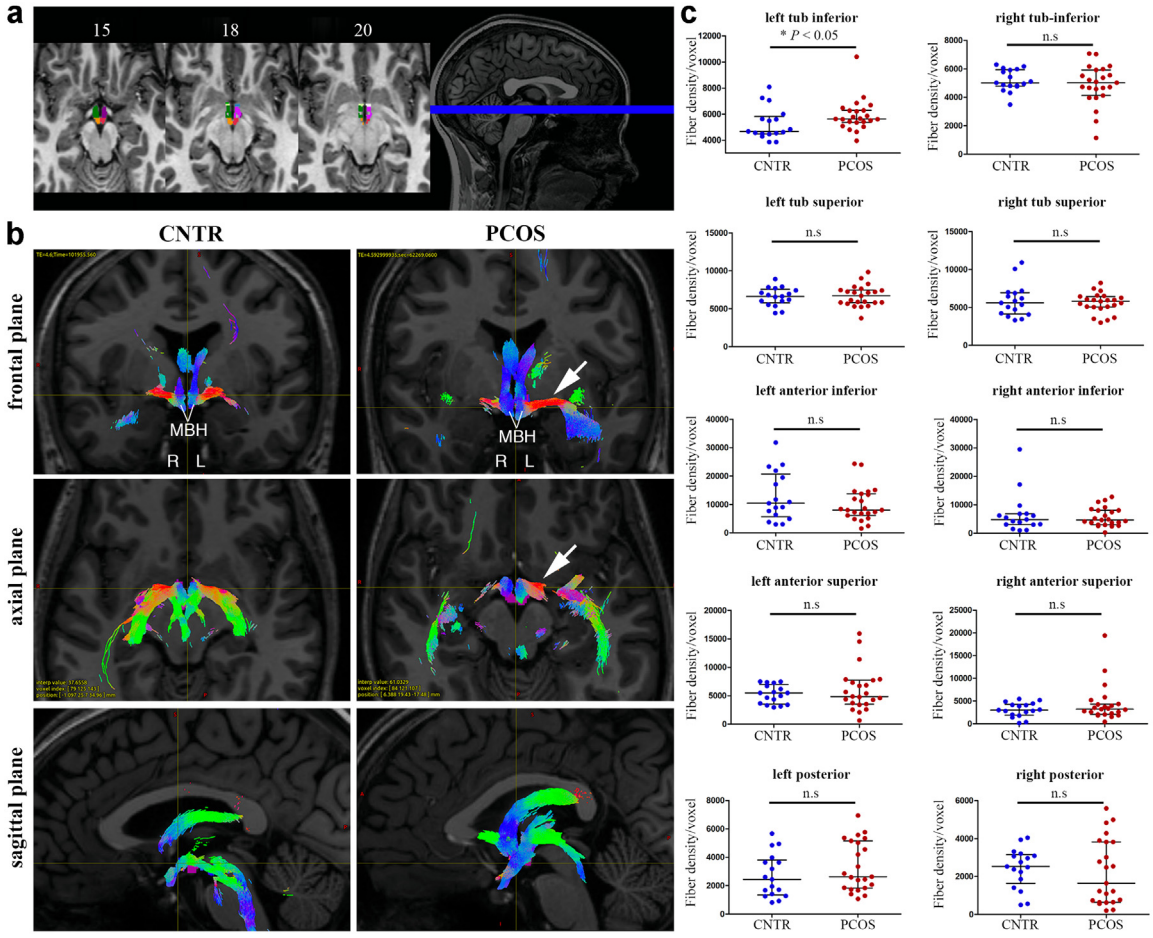

***Fig. 2:* Lateralized asymmetry of the hypothalamic left tubular inferior region in women with PCOS.** (**a**) Radiological view of subunits hypothalamus segmentation with dark green: right tuberal inferior, dark purple: left tuberal inferior, orange: right posterior, pink: left posterior, dark blue: left anterior-inferior, green: right anterior-inferior, light green: right anterior-superior, white: left anterior-superior, light purple: left tubular superior. (**b**) Illustrative examples of fiber tracking through hypothalamus subunits in patients and controls, represented in the 3 major planes. Colors code for fiber directions (blue: inferior-superior, red: left-right, green: anterior-posterior). While fiber density appears symmetrical in the control case, a left-right asymmetry is observed in the PCOS patient with increased connectivity of the left side of the hypothalamus (white arrow). (**c**) Unpaired two-tailed Student's *t* test comparisons between PCOS (n = 23) and controls (n = 17) for fiber density in each hypothalamic subunit; $^*P < 0.05$, n.s: not significant. The horizontal line in each plot corresponds to the median value. The vertical line represents the 25th–75th percentile range.

PCOS-like animals as compared to controls (Fig. 3l; $P < 0.0001$, Wilcoxon–Mann–Whitney test). These data reveal the existence of PCOS-like alterations in ME plasticity in PAMH mice, and raise the possibility that the sustained retraction of tanycytic endfeet could create the permissive environment necessary for GnRH neuron terminals to sprout closer to the pericapillary space and thus increase GnRH secretion into the pituitary portal circulation.

AMH induces morphological plasticity in the ME

To determine whether the increased circulating AMH in PCOS could be responsible for the altered ultrastructural remodeling of the ME, we challenged ME explants from female rats maintained *ex vivo* in artificial cerebrospinal fluid[5,55] with 1 µg/ml AMH or PBS for 30 min, fixed and processed the tissue for immunogold labelling and electron microscopy as above (Fig. 4a). In diestrus II, when GnRH terminals are normally ensheathed by tanycytic processes and are distant from the pericapillary space (Fig. 4b and c), AMH stimulation of ME explants, induced tanycytic processes (green) to retract, allowing GnRH terminals (blue) to sprout closer to the basal lamina (pink) and pericapillary space (Fig. 4d and e). We found a significant reduction in the area occupied by tanycytic processes at less than 2 µm from the basal lamina of AMH-treated explants as compared to controls (Fig. 4f; n = 5 controls, N = 110 number of analysed EM

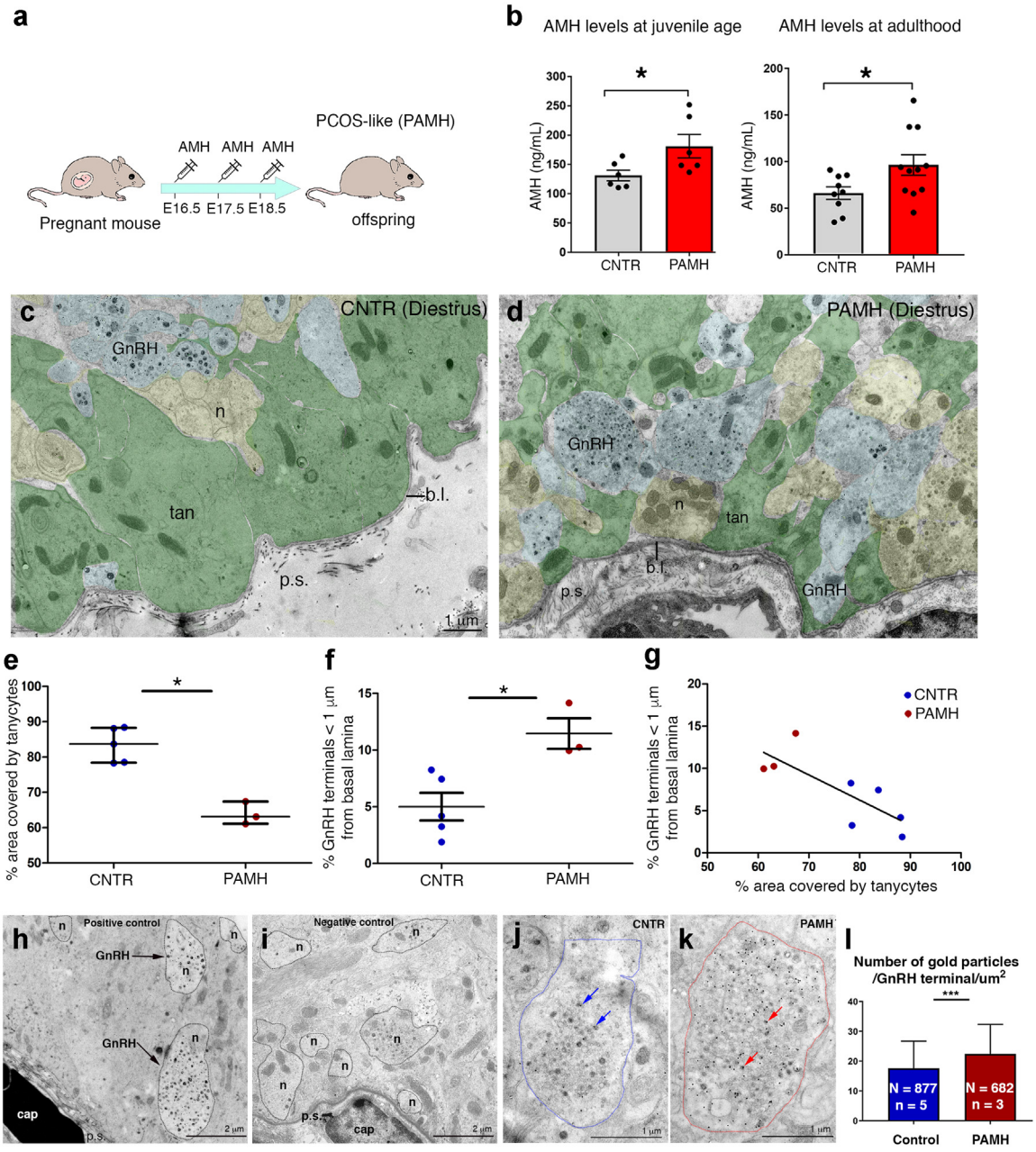

***Fig. 3:* AMH levels and ultrastructural organization of the ME in control and PCOS-animals.** (**a**) Experimental design employed to generate PAMH offspring. (**b**) Blood samples were derived from control and PAMH female mice at postnatal day 25 (P25; *n* = 6 controls, *n* = 6 PAMH) and in adult diestrous animals (2 months; *n* = 9 controls, *n* = 11 PAMH) and AMH concentration was measured by ELISA. Mean AMH levels are significantly higher in PAMH females as compared to control mice (unpaired two-tailed Student's *t* test, **P* < 0.05). Experiments were replicated three times with comparable results. (**c** and **d**) Representative electron micrographs of GnRH-immunoreactive axon terminals (immunogold) from hypothalamic ME dissected from diestrous control (CNTR) or PAMH mice (P90–P120). GnRH axonal endings are highlighted in blue, other neuroendocrine nerve terminals contained in the external layer of the ME are pseudo-coloured in yellow, tanycytic end-feet are pseudo-coloured in green and the pericapillary space (p.s.) in pink. (**e**) Quantitative analysis of the percentage of area occupied by tanycytes in the external zone of the ME at 2 µm from the pericapillary space, in ME explants from CNTR diestrus mice and PAMH mice (**P* < 0.05; Wilcoxon–Mann–Whitney test; *n* = 5 controls, *N* = 58 number of analysed EM photomicrographs in controls; *n* = 3 PAMH mice, *N* = 35 number of analysed EM photomicrographs in PAMH mice). (**f**) Quantitative analysis of the percentage of GnRH nerve terminals located at less than 1 µm from the pericapillary space in the external zone of the ME, in explants from control and PAMH diestrous mice (**P* < 0.05; Wilcoxon–Mann–Whitney test; *n* = 5 controls, *N* = 100 number of GnRH-immunoreactive axon terminals measured per explant in controls; *n* = 3 PAMH mice, *N* = 100 number

photomicrographs in controls; $n = 3$ AMH-treat group, $N = 150$ number of analysed EM photomicrographs in the AMH-treat group; $P < 0.0001$, Wilcoxon–Mann–Whitney test). In addition, the percentage of GnRH axon terminals located less than 1 µm from the pericapillary space was also greater in AHM-treated explants as compared to PBS-treated explants (Fig. 4g; PBS n = 5, AMH n = 3; 100–150 GnRH-immunoreactive axon terminals analysed per explant; $P = 0.03$, Wilcoxon–Mann–Whitney test). This situation is reminiscent of the microstructural changes occurring in the ME under physiological conditions during proestrus, when GnRH release is maximal (Fig. 4h). AMH is thus capable of inducing rapid cytoskeletal changes in the ME that mimic proestrus, resulting in the retraction of tanycytic processes together with the increased proximity of GnRH neuronal terminals to the endothelial wall.

AMH induces morphological remodeling in tanycytes

In order to determine whether this effect of AMH on the structural plasticity of the adult female ME was mediated by tanycytes, we verified whether these cells expressed AMHR2 receptors and/or AMH itself. We began by stereotaxically injecting the Tat-Cre fusion protein[43] into the third ventricle of *tdTomato*$^{loxP/+}$ female mice (Fig. 5a), a method that we have previously shown to selectively lead to reporter fluorescent protein expression in virtually all ME tanycytes, but not in neurons, astrocytes or endothelial cells.[4,56] We then isolated Tomato-positive (tanycytes) and Tomato-negative cells from diestrous explants of mediobasal hypothalamus (MBH), which contains the ME and the ARC, by fluorescence-activated cell sorting (FACS; Fig. 5a) and performed quantitative RT–PCR profiling for genes of the AMH signalling pathway. Interestingly, both *AMHR2* and *AMH* were expressed at comparable levels in tanycytes (Tomato-positive) as well as in Tomato-negative cells (Fig. 5b; $n = 6$ Tomato Pos vs $n = 6$ Tomato Neg; *Amh* mRNA $P = 0.12$, *Amhr2* mRNA $P = 0.63$, Wilcoxon–Mann–Whitney test), suggesting that in addition to circulating AMH of ovarian origin, a local source cannot be ruled out.

Next, we performed fluorescent labelling experiments using an antibody directed against the C-terminal region of AMH, which corresponds to the bioactive form of the molecule (Fig. 5c and d). We detected AMH expression in the ARC (Fig. 5c) and a more robust expression in ME tanycytes and their endfeet (arrowheads, Fig. 5d).

To precisely determine the expression pattern of AMHR2 in the ME, we examined the MBH of an AMHR2-EGFP mouse line, which confirmed that ME tanycytes do indeed express AMHR2 (Fig. 5e and f).

Finally, to confirm that AMH could directly act on ME tanycytes and modulate their ability to periodically extend or retract their endfeet during the estrous cycle, we generated primary cultures of tanycytes from the rat ME (Fig. 5g), which we have previously characterized.[4,42,56]

We further verified the expression of AMH and AMHR2 in these primary tanycytes by western blotting (Fig. 5h), confirming the validity of this *in vitro* model. Next, we inflicted a scratch wound on a monolayer of primary tanycytes and treated the cells for 48 h with either PBS (control) or recombinant hAMH (100 ng/ml). The AMH concentration was chosen based on previous *in vitro* studies from our group.[24,57] At the end of the stimulation period, the cultures were fixed and labelled for the cytoskeletal protein F-actin (Fig. 5i and j). AMH treatment did indeed stimulate cytoskeletal remodeling in tanycytes, inhibiting the extension of tanycytic processes (Fig. 5k; $n = 13$ control vs $n = 17$ AMH-treated; $P = 0.0007$, Wilcoxon–Mann–Whitney test).

Together, these findings indicate that tanycytes could be both responsible for and/or respond to cyclic fluctuations in AMH levels under physiological conditions, thus controlling the proximity of GnRH neurons to the pituitary portal circulation and the pattern and level of GnRH secretion.

Discussion

The reproductive cycle of mammals is critically regulated by hypothalamic GnRH neurons,[58] whose axons in

of GnRH-immunoreactive axon terminals measured per explant in PAMH mice). The horizontal line in each plot corresponds to the median value. The vertical line represents the 25th–75th percentile range. (**g**) Correlation of % of GnRH terminals located at less than 1 µm from the pericapillary space versus the % of area occupied by tanycytes in the external zone of the ME at 2 µm from the pericapillary space ($r = -0.8$, $P = 0.015$, Spearman's correlation). (**h**) Electron microscopic image of GnRH-positive terminals (arrows) in the median eminence located in proximity of the portal capillary basal lamina. (**i**) Electron microscopic image at the same magnification as **h** showing the lack of gold particles in an ultra-thin section of the median eminence after omission of the primary antibody. (**j** and **k**) Representative electron micrographs of GnRH-immunoreactive axon terminals from hypothalamic ME of diestrous control (CNTR) and PAMH mice (P90–P120). Dotted lines depict the surface of a GnRH terminal in a CNTR mouse (blue dotted lines, **j**) and in a PAMH mouse (red dotted lines, **k**). Arrows point to individual 18 nm gold particles showing immunogold labelling in large dense-core vesicles. (**l**) Quantitative analysis of the number of gold particles contained in the GnRH terminals ($n = 5$ controls, $N = 877$ number of GnRH terminals analysed in control mice; $n = 3$ PAMH, $N = 682$ number of GnRH terminals analysed in PAMH mice). Wilcoxon–Mann–Whitney test, ***$P < 0.0001$. The horizontal line in each plot corresponds to the median value. The vertical line represents the 25th–75th percentile range. Abbreviations: b.l., basal lamina; cap, capillary; ME, median eminence; n, neurons; p.s., pericapillary space; tan, tanycytes; EM, electron microscopy.

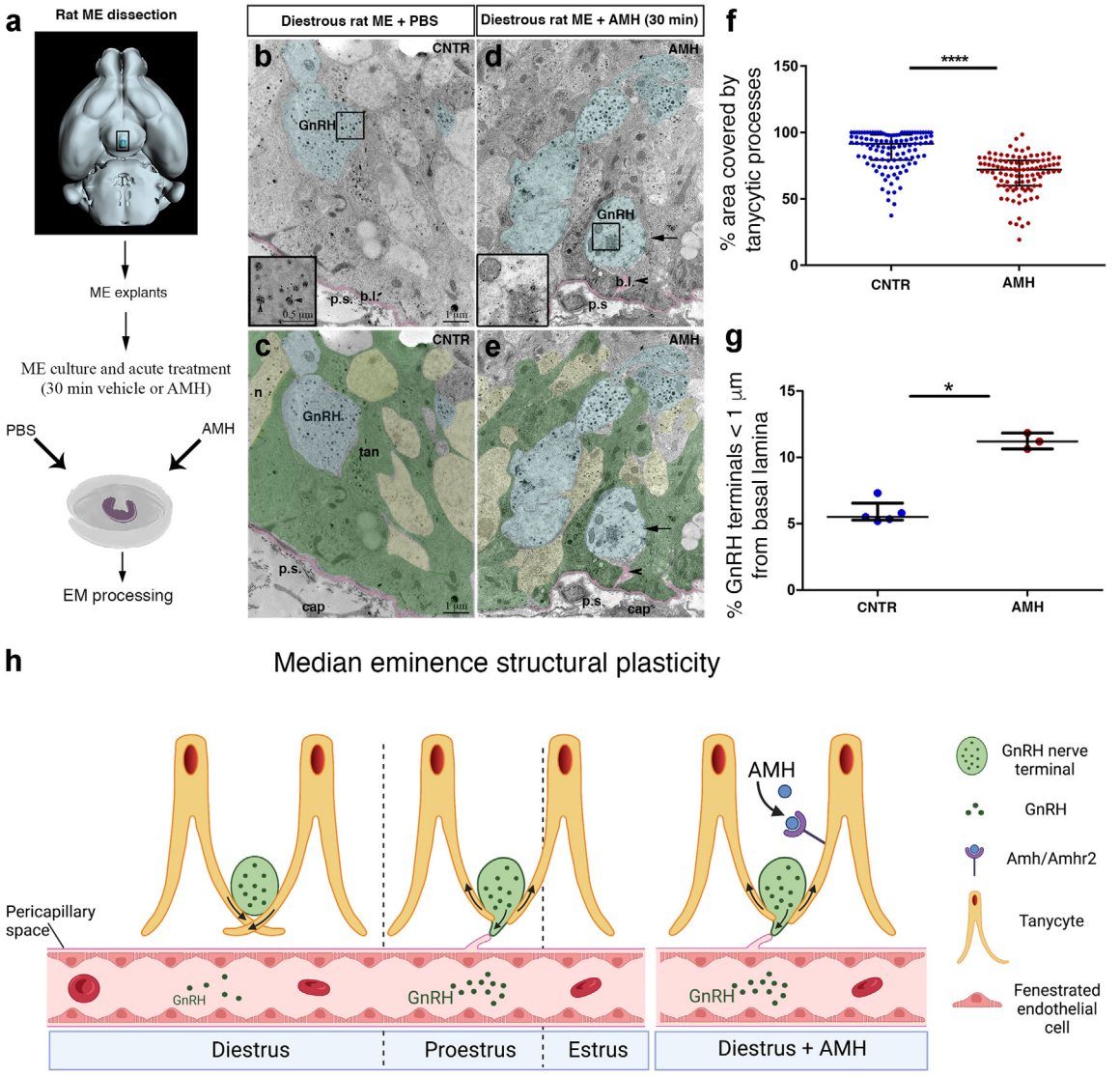

Fig. 4:* AMH induces morphological plasticity in the ME of the adult female brain.** (**a**) Schematic representation summarizing the different steps of the EM experiments. (**b**–**e**) Representative electron micrographs of GnRH-immunoreactive axon terminals (immunogold) from hypothalamic explants containing the ME of female rat in diestrus, incubated in the absence (**b** and **c**) or the presence (**d** and **e**) of AMH_C (1 µg/ml) for 30 min. GnRH axonal endings are pseudo-coloured in blue and the pericapillary space (p.s.) in pink. Insets in **b** and **d** are high-magnification views of boxes drawn in **b** and **d**. Arrowheads in insets point to GnRH-immunoreactive vesicles. (**c** and **e**) Photomicrographs were filled with pseudocolors to highlight respectively the GnRH terminals (blue), other neuroendocrine nerve terminals contained in the external layer of the ME (yellow), the pericapillary space (p.s.) in pink and the tanycytic end-feet (green). (**f**) Quantitative analysis of the percentage of area occupied by tanycytes in the external zone of the ME at 2 µm from the pericapillary space, in explants from rats in diestrus treated or not with AMH_C (*$P < 0.0001$; Wilcoxon–Mann–Whitney test; $n = 5$ controls, $N = 110$ number of analysed EM photomicrographs in controls; $n = 3$ AMH-treat group, $N = 150$ number of analysed EM photomicrographs in the AMH-treat group). (**g**) Quantitative analysis of the percentage of GnRH nerve terminals located at less than 1 µm from the pericapillary space in the external zone of the ME, in explants from rats in diestrus treated or not with AMH_C (*$P < 0.05$; Wilcoxon–Mann–Whitney test; $n = 5$ controls, $N = 110$ number of GnRH-immunoreactive axon terminals measured per explant in controls; $n = 3$ AMH-treat group, $N = 150$ number of GnRH-immunoreactive axon terminals measured per explant in the AMH-treat group). The horizontal line in each plot corresponds to the median value. The vertical line represents the 25th–75th percentile range. (**h**) Schematic representation of the micro-structural changes occurring periodically in the ME during the different phases of the estrous cycle and in diestrous ME explants treated in acute with AMH. Abbreviations: b.l., basal lamina; cap, capillary; EM, electron microscopy; ME, median eminence; n, neurons; p.s., pericapillary space; tan, tanycytes.

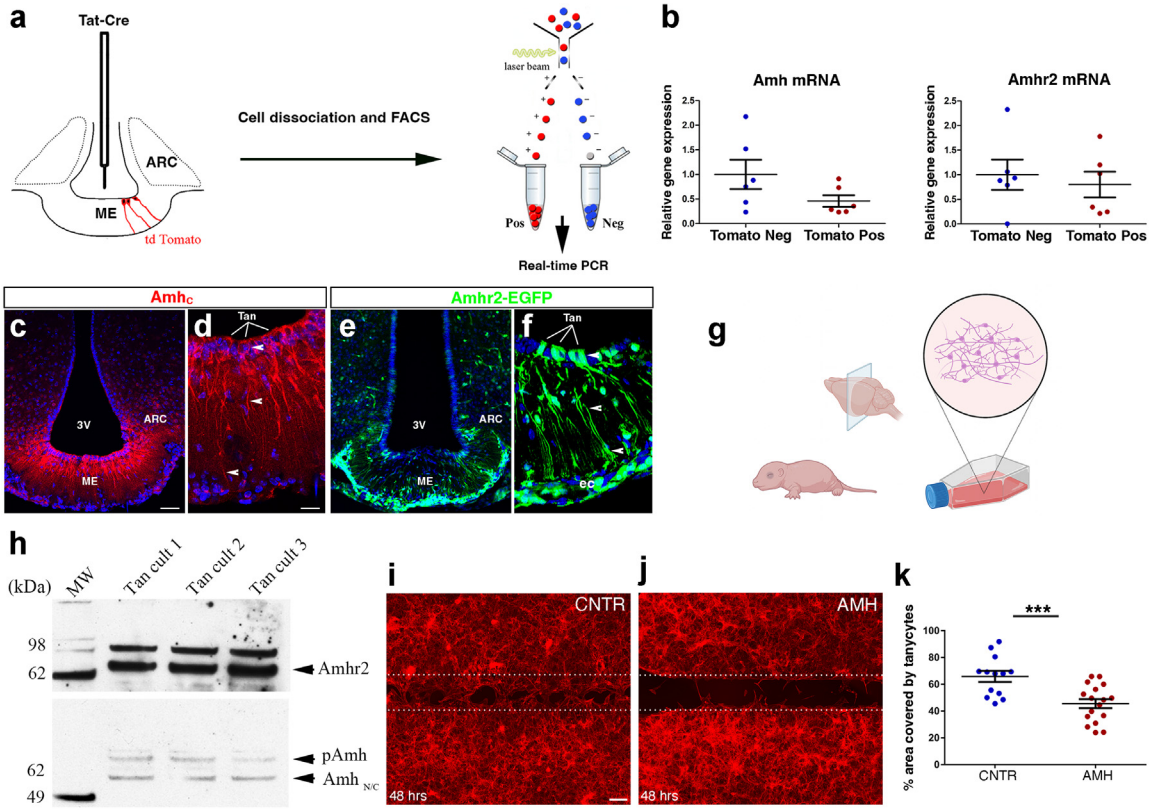

Fig. 5: **Expression of AMH and AMHR2 in ME tanycytes.** (**a**) Tanycyte isolation by FACS and real-time PCR analysis in Tomato-positive (pos; tanycytes) and -negative cells (neg) in *tdTomato*$^{loxP/+}$ mice infused i.c.v. with Tat-cre. Tat-cre injection into the third ventricle results in Cre-Lox recombination (red) exclusively in tanycytes. (**b**) Real-time PCR analysis of indicated genes in tanycytes isolated from Tat-cre;*tdTomato*$^{loxP/+}$ mice, normalized to values in Tomato-negative cells (n = 6 Tomato Pos and n = 6 Tomato Neg; *P < 0.05, **P < 0.005, Wilcoxon–Mann–Whitney test). The horizontal line in each plot corresponds to the median value. The vertical line represents the 25th–75th percentile range. (**c** and **d**) Representative immunofluorescence experiment for AMH$_C$ in coronal sections of the mouse ME depicting AMH expression in ME tanycytes and along their processes (n = 3 brains for each experiment, 3- to 4-month-old female mice. Experiments were repeated three times). (**e** and **f**) AMHR2 expression was analysed in coronal sections of ME of *AMHR2-Cre;Z/E*$^{loxP/-,\beta geo/+}$ (*AMHR2-EGFP*) knock-in reporter line (n = 3 brains for each experiment, 3- to 4-month-old female mice. Experiments were done in triplicates). EGFP is expressed by tanycytes (Tan), endothelial cells (ec) and by cells of the arcuate nucleus (ARN). Scale bars, (**c** and **e**) 50 µm; (**d** and **f**) 20 µm. (**g**) Schematic representing the generation of primary tanycytic cultures. (**h**) Western blotting for AMH and AMHR2 in rat tanycytic primary cultures. (**i** and **j**) Representative photomicrographs of a scratch-wound-healing assay performed on primary tanycytes treated or not for 48 h with recombinant AMH (100 ng/ml; n = 5 independent experiments). Dotted lines indicate the borders of the scratch. After 48 h of exposure to AMH, tanycytes invade a greater area of the scratch in control cultures (PBS-treated; **i**) than in AMH-treated cultures (**j**). Tanycytes were stained using F-actin (red). Scale bars, (**i** and **j**) 100 µm. (**k**) Quantitative analysis of the % area covered by tanycytes in control and AMH-treated conditions (n = 13 Control and n = 17 AMH-treated; ***P < 0.0005, Wilcoxon–Mann–Whitney test). The horizontal line in each plot corresponds to the mean value. The vertical line represents the S.E.M.

the ME periodically sprout towards the pericapillary space, into which they release the GnRH hormone during a specific time window.[6,59] Over the past two decades, it has become clear that GnRH terminals of the ME undergo dynamic transformations as a function of fluctuating physiological conditions[4–6] as well as gonadectomy,[59] which influence the distance between GnRH terminals and the basal lamina. We have recently shown that peripherally administered AMH enters the ME and acts centrally to induce GnRH neuronal activation and secretion.[20] Here, using *in vitro* and *ex-vivo* approaches, we have uncovered a central role for AMH in the regulation of GnRH secretion by the control of cytoskeletal plasticity in tanycytes, by inducing the rapid retraction of AMHR2-expressing tanycytic endfeet, thus allowing GnRH neuron terminals to contact the pericapillary space and release the hormone at the level of the pituitary portal vessels. By favoring GnRH axonal growth in the adult brain, AMH could thus play an important physiological role in orchestrating the central control of reproduction. In addition, since AMHR2 is also expressed in tanycytes and in energy sensing ARC

neurons, it would be interesting in the future to assess whether AMH signalling could be involved in the regulation of energy homeostasis and in the central insulin and/or glucose-sensitivity in physiological conditions as well as in metabolic disturbances such as those associated with PCOS.

Most AMH is secreted by ovarian granulosa cells as a homodimeric precursor made up of two 70-kDa monomers.[27] The precursor consists of two parts: a pro-region that it is important for the synthesis and extracellular transport of AMH, and a 25-kDa COOH-terminal dimer (AMH_C) that becomes bioactive after proteolytic cleavage, allowing it to bind to AMHR2.[60] Circumventricular organs, such as the ME, contain fenestrated endothelial cells that allow the passage of molecules smaller than 35 kDa,[61,62] thus permitting circulating AMH_C to bypass the blood–brain barrier and directly access not only GnRH neurons[20] but tanycytic endfeet in the ME.[62] In this report, however, we show that in the brain of adult female rodents, the MBH is itself a source of AMH as neurons of the ARC and tanycytes express detectable levels of AMH. Whether the AMH is of central or peripheral origin, its effects on these dual targets would be to ramp up GnRH release and, consequently, LH secretion, either during the preovulatory surge or when AMH levels are pathologically elevated, as in PCOS.

Indeed, one key neuroendocrine aberration in women with PCOS is increased LH pulse frequency, documented in 75% of women with PCOS, regardless of their body mass index (BMI).[11,63–65] In these women, LH hyper-pulsatility likely contributes to increased ovarian thecal androgen secretion and the failure of ovulation, constituting a pivotal pathogenic element in the syndrome.[66] In a previous investigation, we provided evidence that, similar to women with PCOS, PAMH mice are also characterized by increased GnRH neuronal activity and LH pulse frequency.[20] These changes are not merely cyclic, since we observe an increase in the percentage of GnRH axonal terminals located in close proximity of the ME capillary network even during diestrus. In addition, these defects are accompanied by higher GnRH content at the level of the axon terminals in our PCOS-like model as compared to controls. Further phenocopying both PCOS patients and the prepubertal daughters of women with PCOS,[29,67,68] in this study, we identified the presence of elevated circulating AMH levels both in juvenile and in adult PAMH mice, indicating that this model may also reproduce the etiology of PCOS.

The origin of GnRH hypersecretion in PCOS is most likely multifactorial. Over the past two decades, it has become clear from preclinical studies that the dynamic transformation of GnRH terminals in the ME takes place not only as a function of fluctuating physiological conditions,[4–6] which influence the distance between GnRH terminals and the basal lamina, but also of gonadectomy.[59] In addition to impairments in the homeostatic feedback mechanism between the gonads and the brain, GnRH neuronal hyperactivity in PCOS might also be the result of alterations in the hypothalamic network regulating GnRH neuron activity[21] and possibly other central mechanisms. Precisely what roles AMH plays in these interconnected mechanisms is yet to be discovered, but it is entirely plausible that a sustained elevation of AMH levels and the resulting loss of neuroglial plasticity, such as seen in female PAMH mice above, would lead to reciprocal long-term morphological changes in the hypothalamus. In line with this supposition, we report a significant increase in hypothalamic neuronal activity and/or axon-glial signalling, as indicated by the increase in the metabolite NAA,[49,50] in women with PCOS. We acknowledge that such interpretation is based on the assumption that the total creatine level (creatine + phospho-creatine) does not change in the hypothalamus of women with PCOS. Unfortunately, there are no previous data available in the literature evaluating the absolute concentration of creatine in the brain of women with PCOS.

Another important consideration to take into account is that, although NAA in brain is an important marker of neuronal function and viability,[69] its variations in content by MRS may be also associated with osmoregulatory stress, neuronal viability, or other multifactorial changes,[70] that could also negatively impact the neuroendocrine responses in the PCOS brain. This raises the possibility that the hypothalamic NAA difference observed in the hypothalamus of women with PCOS could reflect more than just one alteration, which may also vary in relationship to the heterogeneous presentation of PCOS traits. It would be important in the future conducting similar studies in larger cohorts of women with PCOS, segregating endocrine, reproductive and metabolic phenotypes and to perform MRS and diffusion tensor imaging (DTI) measurements in rodent models of PCOS.[53] Indeed, similar MRS and DTI changes as those observed in women with PCOS could be assessed and confirmed in rodent models of PCOS combining high resolution 9.4T MRI imaging with histopathological approaches. This would have the benefit to directly assess changes in hypothalamic activity and axonal-glial modifications in PCOS-like animals and to deeply investigate intracerebral connectivity between the hypothalamus with different brain areas involved in the control of energy homeostasis, reproduction and behaviour (emotion, motivation, memory).

While structural changes in the hypothalamus are known to occur across the ovarian cycle in humans[31] as well as in other species,[71] whether hormonal imbalances in women with PCOS also lead to structural and functional hypothalamic alterations was not previously known. In addition, recent studies have focused on brain structure and activity in women with PCOS in relation to cognitive performance and memory tasks,[72–74] but none of these studies examined the

hypothalamus, a region crucially involved in detecting and integrating reproductive and metabolic signals. The development of advanced central nervous system imaging techniques has proven invaluable for our understanding of the neuroendocrine origins of PCOS and its comorbidities.[75]

In this work, in addition to differences in neuronal activity between PCOS women and controls, we also found a specific lateralized asymmetry in the left inferior tuberal region of women with PCOS as compared with healthy women, consisting of a significantly higher density of fibers crossing this region. This finding directly links PCOS with alterations in the connectivity of the ARC/ME. Interestingly, evidence from preclinical models demonstrates the existence of lateralized asymmetries in the hormonal content in the hypothalamus,[76] and gonadal hormones may have laterally asymmetric effects on the brain as a function of specific developmental time windows.[77] The finding that prenatal exposure to androgen excess in a variety of animal models consistently replicates a wide range of PCOS symptoms in the offspring provides strong evidence that hyperandrogenism is a major driver of pathogenesis,[53] and raises the intriguing question as to whether prenatal androgen excess could be responsible for organizational anomalies in ARC neurocircuitry and the lateralized hypothalamic asymmetry that we observed in women with PCOS.

We recognize limitations in our study as we included in the MRI protocol women under hormonal contraceptive treatment from both groups (10 out of 17 healthy women and 11 out of 23 women with PCOS). We did not perform an exploratory subgroup analysis to further investigate this study limitation because the proportion of patients under oral contraception was approximately the same in both groups: 47.8% (11/23) for the PCOS group and 58.8% (10/17) for the controls (with a χ^2 not statically different). A subgroup analysis did not seem appropriate because of the small numbers of patients involved.

Hormonal contraceptive treatment might have masked the role of AMH on GnRH secretion in women since contraception lowers LH, FSH and E2 even one week after interruption of these treatments,[78] which may explain the lack of difference in serum levels of LH between women with PCOS and controls. Moreover, we should also highlight the fact that women with PCOS often exhibit a more accelerated LH pulse secretion as compared to healthy women,[16–18] without necessarily having higher mean circulating LH levels. Indeed, previous studies have shown that 30%–50% of patients with PCOS exhibit high mean LH levels, which are also modulated by the metabolic status of women with PCOS, as shown in clustering metabolic analyses.[79] In the present study, we did not have access to the information concerning the metabolic status of women with PCOS, with the exception of their BMI. Unfortunately, our ethical authorization precluded frequent blood sampling (at 10 min interval for 8–12 h) required to measure LH pulse frequency in control and PCOS women. Therefore, we could not assess whether women with PCOS that underwent MRI in this study may have an accelerated LH pulse frequency associated with their hypothalamic functional and structural changes, despite normal mean LH values.

However, despite these limitations in LH measurements, women with PCOS presented significantly higher AMH levels and functional hypothalamic alterations than healthy subjects, supporting the notion of increased neuronal activity/axonal-glial signalling in PCOS. It would thus be necessary in the future to perform similar investigations in larger cohorts of PCOS patients, clustering endocrine characteristics related to risk and severity of PCOS with associated metabolic alterations and with frequent blood sampling for repeated hormonal measurements.

In summary, our experiments provide insights into the pathophysiology of this syndrome and identify molecular pathways that could become future therapeutic targets for the treatment of PCOS. Finally, this work also uncovers the potential for structural and metabolic MRI in the hypothalamus as important tools for better understanding the pathophysiology of PCOS.

Contributors

A.-L.B. designed and performed the experiments, analysed the data, and was involved in all aspects of manuscript preparation; N.e.H.M., A.B., D.M., M.S.B.S., V.S., Q.Y., M.C., F.D.B. and C.M. performed experiments and analysed the data; G.K., R.V., R.L. and J.-P. P. performed MRI scans of the patients, analysed the data, reviewed and edited the manuscript; S.R. edited the manuscript; U.B. helped with the analysis and interpretation of the results and preparation of the manuscript; P.P. performed the biochemical analyses of the humans subjects involved in the study, reviewed and edited the manuscript; D.D. reviewed and edited the manuscript and was involved in all aspects of the manuscript preparation; S.C.-J. recruited the patients, provided clinical information for the human study and was involved in all aspects of the manuscript preparation; V.P. was involved in the interpretation of the results and preparation of the manuscript; P.G., A.-L.B. and S.C.-J. designed the study, analysed and verified the underlying data and wrote the manuscript. All authors critically read and commented on the manuscript and approved the final version for submission.

Data sharing statement

Study protocol and all data collected for the study, including raw data and data analysis will be made available to others upon request. All data will be available upon publication of the manuscript, by contacting the corresponding author.

Declaration of interests

A.-L.B. received a honorarium from Merck-Serono for a booklet writing on the use of AMH in Assisted Reproductive Technology; G.K. was a recipient of a Research Grant from Société Française de Neuroradiologie that covered part of his salary.

All the other authors have declared that no conflict of interest exists.

Acknowledgments

This work was supported by INSERM (U1172 to P.G. and V.P.), by the European Research Council (ERC) under the European Union's Horizon 2020 research and innovation program (grant agreement n° 725149 to P.G.), and by the CHU de Lille, France (Bonus H, to P.G.).

We thank the BICeL core facility of Lille, Univ. Lille, CNRS, Inserm, CHU Lille, Institut Pasteur de Lille, US 41-UMS 2014-PLBS, F-59000 Lille, France for the access to the animal facility and to the preclinical imaging core facility. We thank the volunteers who participated to the MRI study.

Appendix A. Supplementary data

Supplementary data related to this article can be found at https://doi.org/10.1016/j.ebiom.2023.104535.

References

1 Christian CA, Moenter SM. The neurobiology of preovulatory and estradiol-induced gonadotropin-releasing hormone surges. *Endocr Rev*. 2010;31(4):544–577.
2 Belchetz PE, Plant TM, Nakai Y, Keogh EJ, Knobil E. Hypophysial responses to continuous and intermittent delivery of hypothalamic gonadotropin-releasing hormone. *Science*. 1978;202(4368):631–633.
3 Prevot V, Bellefontaine N, Baroncini M, et al. Gonadotrophin-releasing hormone nerve terminals, tanycytes and neurohaemal junction remodelling in the adult median eminence: functional consequences for reproduction and dynamic role of vascular endothelial cells. *J Neuroendocrinol*. 2010;22(7):639–649.
4 Parkash J, Messina A, Langlet F, et al. Semaphorin7A regulates neuroglial plasticity in the adult hypothalamic median eminence. *Nat Commun*. 2015;6:6385.
5 Giacobini P, Parkash J, Campagne C, et al. Brain endothelial cells control fertility through ovarian-steroid-dependent release of semaphorin 3A. *PLoS Biol*. 2014;12(3):e1001808.
6 Prevot V, Croix D, Bouret S, et al. Definitive evidence for the existence of morphological plasticity in the external zone of the median eminence during the rat estrous cycle: implication of neuro-glio-endothelial interactions in gonadotropin-releasing hormone release. *Neuroscience*. 1999;94(3):809–819.
7 Prevot V, Sharif A. The polygamous GnRH neuron: astrocytic and tanycytic communication with a neuroendocrine neuronal population. *J Neuroendocrinol*. 2022;34(5):e13104.
8 Gonzalez-Martinez D, Hu Y, Bouloux PM. Ontogeny of GnRH and olfactory neuronal systems in man: novel insights from the investigation of inherited forms of Kallmann's syndrome. *Front Neuroendocrinol*. 2004;25(2):108–130.
9 Tsutsumi R, Webster NJ. GnRH pulsatility, the pituitary response and reproductive dysfunction. *Endocr J*. 2009;56(6):729–737.
10 Norman RJ, Dewailly D, Legro RS, Hickey TE. Polycystic ovary syndrome. *Lancet*. 2007;370(9588):685–697.
11 Goodarzi MO, Dumesic DA, Chazenbalk G, Azziz R. Polycystic ovary syndrome: etiology, pathogenesis and diagnosis. *Nat Rev Endocrinol*. 2011;7(4):219–231.
12 Jayasena CN, Franks S. The management of patients with polycystic ovary syndrome. *Nat Rev Endocrinol*. 2014;10(10):624–636.
13 March WA, Moore VM, Willson KJ, Phillips DI, Norman RJ, Davies MJ. The prevalence of polycystic ovary syndrome in a community sample assessed under contrasting diagnostic criteria. *Hum Reprod*. 2010;25(2):544–551.
14 Wild RA, Carmina E, Diamanti-Kandarakis E, et al. Assessment of cardiovascular risk and prevention of cardiovascular disease in women with the polycystic ovary syndrome: a consensus statement by the Androgen Excess and Polycystic Ovary Syndrome (AE-PCOS) Society. *J Clin Endocrinol Metab*. 2010;95(5):2038–2049.
15 Dumesic DA, Lobo RA. Cancer risk and PCOS. *Steroids*. 2013;78(8):782–785.
16 Berga SL, Guzick DS, Winters SJ. Increased luteinizing hormone and alpha-subunit secretion in women with hyperandrogenic anovulation. *J Clin Endocrinol Metab*. 1993;77(4):895–901.
17 Patel K, Coffler MS, Dahan MH, et al. Increased luteinizing hormone secretion in women with polycystic ovary syndrome is unaltered by prolonged insulin infusion. *J Clin Endocrinol Metab*. 2003;88(11):5456–5461.
18 Rebar R, Judd HL, Yen SS, Rakoff J, Vandenberg G, Naftolin F. Characterization of the inappropriate gonadotropin secretion in polycystic ovary syndrome. *J Clin Invest*. 1976;57(5):1320–1329.
19 Rosenfield RL, Ehrmann DA. The pathogenesis of polycystic ovary syndrome (PCOS): the hypothesis of PCOS as functional ovarian hyperandrogenism revisited. *Endocr Rev*. 2016;37(5):467–520.
20 Tata B, Mimouni NEH, Barbotin AL, et al. Elevated prenatal anti-Mullerian hormone reprograms the fetus and induces polycystic ovary syndrome in adulthood. *Nat Med*. 2018;24(6):834–846.
21 Walters KA, Gilchrist RB, Ledger WL, Teede HJ, Handelsman DJ, Campbell RE. New perspectives on the pathogenesis of PCOS: neuroendocrine origins. *Trends Endocrinol Metab*. 2018;29(12):841–852.
22 Silva MS, Prescott M, Campbell RE. Ontogeny and reversal of brain circuit abnormalities in a preclinical model of PCOS. *JCI Insight*. 2018;3(7):e99405.
23 Silva MSB, Desroziers E, Hessler S, et al. Activation of arcuate nucleus GABA neurons promotes luteinizing hormone secretion and reproductive dysfunction: implications for polycystic ovary syndrome. *eBioMedicine*. 2019;44:582–596.
24 Cimino I, Casoni F, Liu X, et al. Novel role for anti-Mullerian hormone in the regulation of GnRH neuron excitability and hormone secretion. *Nat Commun*. 2016;7:10055.
25 Cate RL, Mattaliano RJ, Hession C, et al. Isolation of the bovine and human genes for Mullerian inhibiting substance and expression of the human gene in animal cells. *Cell*. 1986;45(5):685–698.
26 Fanchin R, Schonauer LM, Righini C, Frydman N, Frydman R, Taieb J. Serum anti-Mullerian hormone dynamics during controlled ovarian hyperstimulation. *Hum Reprod*. 2003;18(2):328–332.
27 Barbotin AL, Peigne M, Malone SA, Giacobini P. Emerging roles of anti-Mullerian hormone in hypothalamic-pituitary function. *Neuroendocrinology*. 2019;109(3):218–229.
28 Cook CL, Siow Y, Brenner AG, Fallat ME. Relationship between serum mullerian-inhibiting substance and other reproductive hormones in untreated women with polycystic ovary syndrome and normal women. *Fertil Steril*. 2002;77(1):141–146.
29 Pigny P, Jonard S, Robert Y, Dewailly D. Serum anti-Mullerian hormone as a surrogate for antral follicle count for definition of the polycystic ovary syndrome. *J Clin Endocrinol Metab*. 2006;91(3):941–945.
30 Piltonen TT, Giacobini P, Edvinsson A, et al. Circulating anti-mullerian hormone and steroid hormone levels remain high in pregnant women with polycystic ovary syndrome at term. *Fertil Steril*. 2019;111(3):588–596.e1.
31 Baroncini M, Jissendi P, Catteau-Jonard S, et al. Sex steroid hormones-related structural plasticity in the human hypothalamus. *Neuroimage*. 2010;50(2):428–433.
32 Rotterdam ESHRE/ASRM-Sponsored PCOS Consensus Workshop Group. Revised 2003 consensus on diagnostic criteria and long-term health risks related to polycystic ovary syndrome (PCOS). *Hum Reprod*. 2004;19(1):41–47.
33 Dewailly D, Gronier H, Poncelet E, et al. Diagnosis of polycystic ovary syndrome (PCOS): revisiting the threshold values of follicle count on ultrasound and of the serum AMH level for the definition of polycystic ovaries. *Hum Reprod*. 2011;26(11):3123–3129.
34 Rahman SA, Grant LK, Gooley JJ, Rajaratnam SMW, Czeisler CA, Lockley SW. Endogenous circadian regulation of female reproductive hormones. *J Clin Endocrinol Metab*. 2019;104(12):6049–6059.
35 Florent V, Baroncini M, Jissendi-Tchofo P, et al. Hypothalamic structural and functional imbalances in anorexia nervosa. *Neuroendocrinology*. 2020;110(6):552–562.
36 Provencher SW. Estimation of metabolite concentrations from localized in vivo proton NMR spectra. *Magn Reson Med*. 1993;30(6):672–679.
37 Billot B, Bocchetta M, Todd E, Dalca AV, Rohrer JD, Iglesias JE. Automated segmentation of the hypothalamus and associated subunits in brain MRI. *Neuroimage*. 2020;223:117287.
38 Glasser MF, Sotiropoulos SN, Wilson JA, et al. The minimal preprocessing pipelines for the Human Connectome Project. *Neuroimage*. 2013;80:105–124.
39 Jamin SP, Arango NA, Mishina Y, Hanks MC, Behringer RR. Requirement of Bmpr1a for Mullerian duct regression during male sexual development. *Nat Genet*. 2002;32(3):408–410.
40 Novak A, Guo C, Yang W, Nagy A, Lobe CG. Z/EG, a double reporter mouse line that expresses enhanced green fluorescent protein upon Cre-mediated excision. *Genesis*. 2000;28(3–4):147–155.
41 Beauvillain JC, Tramu G. Immunocytochemical demonstration of LH-RH, somatostatin, and ACTH-like peptide in osmium-postfixed, resin-embedded median eminence. *J Histochem Cytochem*. 1980;28(9):1014–1017.
42 De Seranno S, Estrella C, Loyens A, et al. Vascular endothelial cells promote acute plasticity in ependymoglial cells of the neuroendocrine brain. *J Neurosci*. 2004;24(46):10353–10363.

43 Peitz M, Pfannkuche K, Rajewsky K, Edenhofer F. Ability of the hydrophobic FGF and basic TAT peptides to promote cellular uptake of recombinant Cre recombinase: a tool for efficient genetic engineering of mammalian genomes. *Proc Natl Acad Sci U S A*. 2002;99(7):4489–4494.
44 Casoni F, Malone SA, Belle M, et al. Development of the neurons controlling fertility in humans: new insights from 3D imaging and transparent fetal brains. *Development*. 2016;143(21):3969–3981.
45 Duquenne M, Folgueira C, Bourouh C, et al. Leptin brain entry via a tanycytic LepR-EGFR shuttle controls lipid metabolism and pancreas function. *Nat Metab*. 2021;3(8):1071–1090.
46 Percie du Sert N, Hurst V, Ahluwalia A, et al. The ARRIVE guidelines 2.0: updated guidelines for reporting animal research. *Exp Physiol*. 2020;105(9):1459–1466.
47 van der Spuy ZM, Sohnius U, Pienaar CA, Schall R. Gonadotropin and estradiol secretion during the week of placebo therapy in oral contraceptive pill users. *Contraception*. 1990;42(6):597–609.
48 Ross B, Bluml S. Magnetic resonance spectroscopy of the human brain. *Anat Rec*. 2001;265(2):54–84.
49 Moffett JR, Arun P, Ariyannur PS, Namboodiri AM. N-Acetylaspartate reductions in brain injury: impact on post-injury neuroenergetics, lipid synthesis, and protein acetylation. *Front Neuroenergetics*. 2013;5:11.
50 Moffett JR, Ross B, Arun P, Madhavarao CN, Namboodiri AM. N-Acetylaspartate in the CNS: from neurodiagnostics to neurobiology. *Prog Neurobiol*. 2007;81(2):89–131.
51 Urenjak J, Williams SR, Gadian DG, Noble M. Proton nuclear magnetic resonance spectroscopy unambiguously identifies different neural cell types. *J Neurosci*. 1993;13(3):981–989.
52 Behrens TE, Johansen-Berg H, Woolrich MW, et al. Non-invasive mapping of connections between human thalamus and cortex using diffusion imaging. *Nat Neurosci*. 2003;6(7):750–757.
53 Stener-Victorin E, Padmanabhan V, Walters KA, et al. Animal models to understand the etiology and pathophysiology of polycystic ovary syndrome. *Endocr Rev*. 2020;41(4):bnaa010.
54 Mimouni NEH, Paiva I, Barbotin AL, et al. Polycystic ovary syndrome is transmitted via a transgenerational epigenetic process. *Cell Metab*. 2021;33(3):513–530.e8.
55 de Seranno S, d'Anglemont de Tassigny X, Estrella C, et al. Role of estradiol in the dynamic control of tanycyte plasticity mediated by vascular endothelial cells in the median eminence. *Endocrinology*. 2010;151(4):1760–1772.
56 Balland E, Dam J, Langlet F, et al. Hypothalamic tanycytes are an ERK-gated conduit for leptin into the brain. *Cell Metab*. 2014;19(2):293–301.
57 Malone SA, Papadakis GE, Messina A, et al. Defective AMH signaling disrupts GnRH neuron development and function and contributes to hypogonadotropic hypogonadism. *Elife*. 2019;8:e47198.
58 Herbison AE. Control of puberty onset and fertility by gonadotropin-releasing hormone neurons. *Nat Rev Endocrinol*. 2016;12(8):452–466.
59 King JC, Letourneau RJ. Luteinizing hormone-releasing hormone terminals in the median eminence of rats undergo dramatic changes after gonadectomy, as revealed by electron microscopic image analysis. *Endocrinology*. 1994;134(3):1340–1351.
60 di Clemente N, Jamin SP, Lugovskoy A, et al. Processing of anti-Mullerian hormone regulates receptor activation by a mechanism distinct from TGF-beta. *Mol Endocrinol*. 2010;24(11):2193–2206.
61 Schaeffer M, Langlet F, Lafont C, et al. Rapid sensing of circulating ghrelin by hypothalamic appetite-modifying neurons. *Proc Natl Acad Sci U S A*. 2013;110(4):1512–1517.
62 Prevot V, Dehouck B, Sharif A, Ciofi P, Giacobini P, Clasadonte J. The versatile tanycyte: a hypothalamic integrator of reproduction and energy metabolism. *Endocr Rev*. 2018;39(3):333–368.
63 Morales AJ, Laughlin GA, Butzow T, Maheshwari H, Baumann G, Yen SS. Insulin, somatotropic, and luteinizing hormone axes in lean and obese women with polycystic ovary syndrome: common and distinct features. *J Clin Endocrinol Metab*. 1996;81(8):2854–2864.
64 Taylor AE, McCourt B, Martin KA, et al. Determinants of abnormal gonadotropin secretion in clinically defined women with polycystic ovary syndrome. *J Clin Endocrinol Metab*. 1997;82(7):2248–2256.
65 Ehrmann DA. Polycystic ovary syndrome. *N Engl J Med*. 2005;352(12):1223–1236.
66 Caldwell ASL, Edwards MC, Desai R, et al. Neuroendocrine androgen action is a key extraovarian mediator in the development of polycystic ovary syndrome. *Proc Natl Acad Sci U S A*. 2017;114(16):E3334–E3343.
67 Pigny P, Merlen E, Robert Y, et al. Elevated serum level of anti-Mullerian hormone in patients with polycystic ovary syndrome: relationship to the ovarian follicle excess and to the follicular arrest. *J Clin Endocrinol Metab*. 2003;88(12):5957–5962.
68 Sir-Petermann T, Codner E, Maliqueo M, et al. Increased anti-Mullerian hormone serum concentrations in prepubertal daughters of women with polycystic ovary syndrome. *J Clin Endocrinol Metab*. 2006;91(8):3105–3109.
69 Xu S, Yang J, Shen J. Measuring N-acetylaspartate synthesis in vivo using proton magnetic resonance spectroscopy. *J Neurosci Methods*. 2008;172(1):8–12.
70 Lei H, Dirren E, Poitry-Yamate C, Schneider BL, Gruetter R, Aebischer P. Evolution of the neurochemical profiles in the G93A-SOD1 mouse model of amyotrophic lateral sclerosis. *J Cereb Blood Flow Metab*. 2019;39(7):1283–1298.
71 Ojeda SR, Ma YJ, Lee BJ, Prevot V. Glia-to-neuron signalling and the neuroendocrine control of female puberty. *Recent Prog Horm Res*. 2000;55:197–223. discussion-4.
72 Rees DA, Udiawar M, Berlot R, Jones DK, O'Sullivan MJ. White matter microstructure and cognitive function in young women with polycystic ovary syndrome. *J Clin Endocrinol Metab*. 2016;101(1):314–323.
73 Soleman RS, Kreukels BPC, Veltman DJ, et al. Does polycystic ovary syndrome affect cognition? A functional magnetic resonance imaging study exploring working memory. *Fertil Steril*. 2016;105(5):1314–1321.e1.
74 Lai W, Li X, Zhu H, et al. Plasma luteinizing hormone level affects the brain activity of patients with polycystic ovary syndrome. *Psychoneuroendocrinology*. 2020;112:104535.
75 Ozgen Saydam B, Yildiz BO. Polycystic ovary syndrome and brain: an update on structural and functional studies. *J Clin Endocrinol Metab*. 2021;106(2):e430–e441.
76 Gerendai I, Csaba Z, Voko Z, Csernus V. Involvement of a direct neural mechanism in the control of gonadal functions. *J Steroid Biochem Mol Biol*. 1995;53(1–6):299–305.
77 Nordeen EJ, Yahr P. Hemispheric asymmetries in the behavioral and hormonal effects of sexually differentiating mammalian brain. *Science*. 1982;218(4570):391–394.
78 Hedon B, Cristol P, Plauchut A, et al. Ovarian consequences of the transient interruption of combined oral contraceptives. *Int J Fertil*. 1992;37(5):270–276.
79 Huang CC, Tien YJ, Chen MJ, Chen CH, Ho HN, Yang YS. Symptom patterns and phenotypic subgrouping of women with polycystic ovary syndrome: association between endocrine characteristics and metabolic aberrations. *Hum Reprod*. 2015;30(4):937–946.